

# Progenitor and close-in circumstellar medium of type II supernova 2020fqv from high-cadence photometry and ultra-rapid UV spectroscopy

Samaporn Tinyanont<sup>1,★</sup>, R. Ridden-Harper<sup>2</sup>, R. J. Foley<sup>1</sup>, V. Morozova<sup>3</sup>, C. D. Kilpatrick<sup>4,5</sup>, G. Dimitriadis<sup>1,6</sup>, L. DeMarchi<sup>4,5</sup>, A. Gagliano<sup>7,8</sup>, W. V. Jacobson-Galán<sup>4,5</sup>, A. Messick<sup>9</sup>, J. D. R. Pierel<sup>10</sup>, A. L. Piro<sup>11</sup>, E. Ramirez-Ruiz<sup>1</sup>, M. R. Siebert<sup>1</sup>, K. C. Chambers<sup>12</sup>, K. E. Clever<sup>1</sup>, D. A. Coulter<sup>1</sup>, K. De<sup>13</sup>, M. Hankins<sup>14</sup>, T. Hung<sup>1</sup>, S. W. Jha<sup>15</sup>, C. E. Jimenez Angel<sup>16,17</sup>, D. O. Jones<sup>1</sup>, M. M. Kasliwal<sup>13</sup>, C.-C. Lin<sup>12</sup>, R. Marques-Chaves<sup>18</sup>, R. Margutti<sup>4,5</sup>, A. Moore<sup>19</sup>, I. Pérez-Fournon<sup>16,17</sup>, F. Poidevin<sup>16,17</sup>, A. Rest<sup>2,10</sup>, R. Shirley<sup>20</sup>, C. S. Smith<sup>1</sup>, E. Strasburger<sup>21</sup>, J. J. Swift<sup>22</sup>, R. J. Wainscoat<sup>12</sup>, Q. Wang<sup>2</sup> and Y. Zenati<sup>2†</sup>

Affiliations are listed at the end of the paper

Accepted 2021 October 1. Received 2021 October 1; in original form 2021 July 30

## ABSTRACT

We present observations of SN 2020fqv, a Virgo-cluster type II core-collapse supernova (CCSN) with a high temporal resolution light curve from the *Transiting Exoplanet Survey Satellite* (*TESS*) covering the time of explosion; ultraviolet (UV) spectroscopy from the *Hubble Space Telescope* (*HST*) starting 3.3 d post-explosion; ground-based spectroscopic observations starting 1.1 d post-explosion; along with extensive photometric observations. Massive stars have complicated mass-loss histories leading up to their death as CCSNe, creating circumstellar medium (CSM) with which the SNe interact. Observations during the first few days post-explosion can provide important information about the mass-loss rate during the late stages of stellar evolution. Model fits to the quasi-bolometric light curve of SN 2020fqv reveal 0.23  $M_{\odot}$  of CSM confined within 1450  $R_{\odot}$  ( $10^{14}$  cm) from its progenitor star. Early spectra (<4 d post-explosion), both from *HST* and ground-based observatories, show emission features from high-ionization metal species from the outer, optically thin part of this CSM. We find that the CSM is consistent with an eruption caused by the injection of  $\sim 5 \times 10^{46}$  erg into the stellar envelope  $\sim 300$  d pre-explosion, potentially from a nuclear burning instability at the onset of oxygen burning. Light-curve fitting, nebular spectroscopy, and pre-explosion *HST* imaging consistently point to a red supergiant (RSG) progenitor with  $M_{ZAMS} \approx 13.5\text{--}15 M_{\odot}$ , typical for SN II progenitor stars. This finding demonstrates that a typical RSG, like the progenitor of SN 2020fqv, has a complicated mass-loss history immediately before core collapse.

**Key words:** stars: massive – stars: mass-loss – supernovae: individual: SN 2020fqv.

## 1 INTRODUCTION

Massive stars ( $\gtrsim 8 M_{\odot}$ ) shed a significant amount of mass towards the end of their lives, forming circumstellar medium (CSM) with variable density profiles, physical extents, and total mass. Physical processes responsible for mass-loss may include stellar winds, minor eruptive mass-loss associated with late-stage nuclear burning instabilities, binary interactions, and likely combinations thereof (Smith 2014, and references therein). However, the rates and quantitative contributions from each of these processes in different types of progenitor stars remain the subject of ongoing research (see e.g. pre-SN instability and outburst, Leung & Fuller 2020; Wu & Fuller 2021; binary effects on stellar structure, Laplace et al. 2020; Zapartas et al. 2021; and new stellar wind prescriptions, Björklund et al. 2021; Kee et al. 2021). Observations of the resulting core-collapse supernova

(CCSN) interacting with the CSM can probe its density structure, providing clues about its origin and the properties of the progenitor star.

CCSNe with a large amount of CSM (a few  $M_{\odot}$ ) close to the progenitor star have been observed for decades, as they are luminous and show persistent interaction signatures (Schlegel 1990). In this scenario, the SN shock collides with the CSM and converts kinetic energy into heat, which gets radiated away as extra luminosity. The spectra of these SNe are classified as Type IIn (Schlegel 1990; Filippenko 1997) with strong and persistent (over months or years) narrow ( $\sim 100\text{--}1000$  km s<sup>-1</sup>) recombination lines from hydrogen in the CSM. There is a rarer class of strongly interacting SNe with only helium lines called Ibn (Matheson et al. 2000; Foley et al. 2007; Pastorello et al. 2007; Pastorello et al. 2008), with a smaller associated CSM mass. More recently, events with a CSM lacking hydrogen and helium are found and classified as Type Icn (Gal-Yam et al. 2021). In addition, some stripped-envelope SNe have been observed to exhibit Type IIn-like spectra at late times, several months post-explosion, indicative of mass-loss centuries before the

\* E-mail: stinyanont@ucsc.edu

† CHE Israel Excellence Fellowship

explosion (e.g. SNe 2001em, Chugai & Chevalier 2006, Chandra et al. 2020; 2004dk, Mauerhan et al. 2018; 2014C, Milisavljevic et al. 2015; Margutti et al. 2017; 2019oys, Sollerman et al. 2020, and 2019yvr, Auchettl et al. in preparation). These strongly interacting SNe are also bright and long-lasting in the infrared (IR), with some remaining detected decades after the explosion (e.g. Fox et al. 2011; Tinyanont et al. 2016, 2019b). While readily detectable, these strongly interacting SNe represent only about 10 percent of all CCSNe (Smith et al. 2011). They are products of progenitor systems with the most extreme mass-loss, such as Luminous Blue Variables (LBVs), extreme red supergiants (RSGs) with eruptive mass-loss, or interacting binary systems (Smith, Hinkle & Ryde 2009; Foley et al. 2011; Margutti et al. 2014; Smith 2017, and references therein).

For the majority of CCSNe, weaker signs of CSM interaction are present but have escaped scrutiny for decades until the recent advent of large-scale transient surveys that discover a large number of SNe, some at very early times. These surveys include the All-Sky Automated Survey for SuperNovae (ASAS-SN; Shappee et al. 2014), the Asteroid Terrestrial-impact Last Alert System (ATLAS; Tonry et al. 2018), the Young Supernova Experiment (YSE; Jones et al. 2021), and the Zwicky Transient Facility (ZTF; Bellm et al. 2019). For dense and nearby CSM from mass-loss immediately before the SN, the energetic shock breakout (SBO) emission radiatively ionizes the CSM, producing narrow Balmer series, He I, and highly ionized metallic emission lines with pronounced electron-scattering Lorentzian wings. These so-called flash ionization features only last for hours to days as the CSM recombines or gets overrun by the SN shock; thus, they are missed in SNe with no early observations. Examples of CCSNe exhibiting these features include SNe 2013cu (Gal-Yam et al. 2014), 2013fs (Yaron et al. 2017), 2017ahn (Tartaglia et al. 2021), 2020pni (Terreran et al. 2021), and 2020tlf (Jacobson-Galán et al. 2021).

While the flash ionization features are ephemeral, CSM interaction can produce excess flux in the light curve of the SN up to  $\sim$ month post-explosion. Such early-time bolometric luminosity excess has been observed in many CCSNe, including the nearby and well-studied SNe 2017eaw (Morozova et al. 2020) and 2018cuf (Dong et al. 2021). In some events, like SN 2017gmr (Andrews et al. 2019), the excess flux from the CSM can be present without early-time flash ionization features. Morozova, Piro & Valenti (2018) demonstrated using light curves of 20 nearby hydrogen-rich (Type II) SNe that early-time excess flux from CSM interaction is a generic feature of this class of CCSNe. In addition to photometric evidence, there is also spectroscopic evidence of high-velocity absorption features from hydrogen and helium caused by the continuous excitation of the outermost ejecta by ongoing CSM interactions (Chugai, Chevalier & Utrobin 2007) in many SNe II-P (SNe II with a luminosity plateau) (e.g. Gutiérrez et al. 2017; Dastidar et al. 2019; Davis et al. 2019; Tinyanont et al. 2019a; Dong et al. 2021). Because SNe II-P are explosions of normal RSGs (see review by Smartt 2009), the ubiquity of CSM interaction in SNe II-P indicates enhanced mass-loss in these stars towards the end of their life, perhaps due to the instability in late-stage nuclear burning (Quataert & Shiode 2012; Fuller 2017).

Observing and constraining CSM properties of SNe II-P can help us better understand the evolution of RSGs prior to their death, and help us answer some unresolved problems in massive stellar evolution. For instance, one of the most contentious issues is the ‘RSG problem’, which is the apparent lack of high-mass ( $>17 M_{\odot}$ ) RSG progenitors to SNe II-P, despite the presence of RSGs in this mass range in the local universe (Smartt et al. 2009; Smartt 2015). There are many possible solutions to this problem. RSGs in this mass range may experience a direct collapse into a black hole,

producing no SN (e.g. O’Connor & Ott 2011; Adams et al. 2017; Sukhbold & Adams 2020). There may be biases with progenitor mass measurements from pre-explosion imaging alone; some studies inferring the progenitor mass from star formation histories found that high-mass RSGs can produce CCSNe (e.g. Jennings et al. 2014; Auchettl et al. 2019). Alternatively, RSGs with high  $M_{ZAMS}$  may shed their hydrogen envelopes and evolve to another stellar type before explosion, explode in environments with high circumstellar or interstellar extinction (Walmswell & Eldridge 2012; Kilpatrick & Foley 2018), explode as another CCSN type (e.g. SN II in Smith 2014), or some combination of all of these. Relatedly, the explosions of stars with high  $M_{ZAMS}$  may be veiled by the very same dusty CSM and are missed by optical transient surveys (Jencson et al. 2019). Lastly, Davies & Beasor (2018, 2020) argue that the RSG problem is not statistically significant, since there are considerable uncertainties in the mass (and luminosity) measurements of progenitor RSGs, especially in the sampling of their spectral energy distributions and the bolometric corrections assumed. To further complicate this discussion, binary interaction, which is common in massive stars including RSGs, affects the mass evolution of an SN progenitor from  $M_{ZAMS}$  to the pre-explosion mass (Zapartas et al. 2019, 2021). Thus, a continued effort to follow-up SNe II-P to constrain their progenitor properties, in conjunction with surveys to find disappearing RSGs (e.g. Adams et al. 2017), is required to understand the fate of high-mass RSGs.

Here, we present observations and data analysis of the nearby Type II-P SN 2020fqv, focusing on its progenitor star and CSM properties. The SN was discovered on 2020 April 1 (ZTF20aatzhhl; Forster et al. 2020; UT time used throughout the paper), in NGC 4568. The SN was monitored by the *Transiting Exoplanet Survey Satellite* (*TESS*; Ricker et al. 2015), covering its explosion and subsequent rise. While it was originally classified as an SN II (likely IIb; Zhang et al. 2020), our light curves (Section 2.5) show a distinct luminosity plateau and our spectra (Section 2.7) show hydrogen at all phases, indicating that it is a Type II-P SN. We executed ultra-rapid target of opportunity (ToO) observations of the SN with the *Hubble Space Telescope* (*HST*); the first ultra-rapid ToO observations ever performed. We note that all epochs mentioned in this paper are relative to the explosion date derived in Section 3.2. Fig. 1 shows the location of the SN in the host galaxy.

The distance to NGC 4568 was not well constrained in the studies of previous CCSNe 1990B (Ib) and 2004cc (Ic) (e.g. van Dyk et al. 1993; Clocchiatti et al. 2001; van den Bergh, Li & Filippenko 2005), with assumed distances ranging from the distance to the Virgo cluster ( $\sim 16$  Mpc) to the distance based on its redshift ( $\sim 32$  Mpc). For this work, we adopt a distance derived from the Tully-Fisher relation in the near-IR of  $17.3 \pm 3.6$  Mpc (Theureau et al. 2007), consistent with being a Virgo cluster member.<sup>1</sup> Given SN 2020fqv’s proximity and early detection, this SN presents another opportunity to probe the properties of close-in CSM around a common SN II-P.

In Section 2, we summarize the observations obtained for this SN. In Section 3, we present different data analyses performed on the SN data. We discuss the construction of the quasi-bolometric light curve and the analysis of the *TESS* light curve. We determine the explosion and CSM parameters from our photometric observations.

<sup>1</sup>We note that while Theureau et al. (2007) lists a corrected kinematical distance to NGC 4568 as 32.2 Mpc, they commented that the method they used to derive this figure assumes the redshift distance as a starting point and does not work well for galaxies in clusters.



**Figure 1.** False-colour image of SN 2020fqv in its host galaxy system NGC 4567 and 4568. The location of the SN is shown in the inset. The image is composed of a pre-explosion single-band *HST*/WFPC2 image in the F606W filter with the colour information from ground-based images obtained using the Nickel Telescope at Lick Observatory. The image of the SN and the area outside of *HST* field of view is also from Nickel. Image credit: Joseph Depasquale/STScI.

We analyse early-time UV spectra and optical nebular spectra. Finally, we provide discussions and conclusions in Section 4.

## 2 OBSERVATIONS

### 2.1 Rapid early-time observations

Immediately after the discovery and classification of SN 2020fqv as a young nearby SN II in an active *TESS* sector were announced, we activated our follow-up observation resources to capture the first few days of its evolution. We obtained the first optical spectrum on 2020 April 01 00:44 (26 h post-explosion). Following this and the public classification of SN 2020fqv at 2020 April 01 16:15 (Zhang et al. 2020) (42 h post-explosion), we notified the Space Telescope Science Institute (STScI) within 50 min (at 17:04 on the same day) of our intention to trigger our disruptive target of opportunity (ToO) programme to observe it with *HST*. The phase 2 observation plans were submitted at 18:45, and the ToO trigger was submitted at 19:14. Finally, we informed STScI that the observations were ready to be executed at 21:21. The first *HST*/STIS observation began on 2020 April 03 at 05:36, a mere 32 h after the ToO trigger was submitted, 37 h after the SN’s classification, and 79 h after the explosion. Fig. 2 summarizes the timeline of the early observational sequence of SN 2020fqv along with the light curves from *TESS* and ground-based observatories described later in this section.

### 2.2 Ultraviolet spectroscopy

We triggered ultra-rapid UV spectroscopy observations of SN 2020fqv with *HST* as part of the Ultra-Rapid UV Spectroscopy

of an Interacting Supernova Discovered by *TESS* program (GO-15876; PI: Foley) due to its proximity and youth at the time of discovery along with its location within *TESS*’s active sector and signs of interaction from the classification spectrum (Dimitriadis et al. 2020). *HST* observed the SN at five epochs from 3 to 17 d post-explosion, using the Space Telescope Imaging Spectrograph (STIS) and Cosmic Origin Spectrograph (COS), providing the wavelength coverage between 1300 and 4000 Å. Table 1 summarizes the *HST* observations. The COS observations were available only for day 5, in two different gratings. Another epoch of COS observation was attempted on day 11, but resulted in no data.

The data were reduced using the standard STIS and COS data reduction pipelines, *STISTOOLS*<sup>2</sup> and *CALCOS*,<sup>3</sup> respectively. Fig. 3 shows the STIS and COS spectra. For STIS, the blue channel spectra on days 3.4 and 5.6 were taken with the CCD and the G230LB grating while those on days 4.9, 11, and 17 were taken with the NUV-MAMA detector and the G230L grating. The spectra were corrected for dust extinction using the parameters derived in Section 3.1 and the Fitzpatrick (1999) dust extinction law. We used the package *EXTINCTION* to deredden the data.<sup>4</sup> The spectra shown are binned for visualization. The red ( $\lambda \gtrsim 3000$  Å) and the blue MAMA data were binned by 3 pixels while the blue CCD data were binned by 5 pixels. The COS spectra were obtained on day 5 using the G130M and G160M gratings. They only show non-detection.

<sup>2</sup><https://stistools.readthedocs.io/>

<sup>3</sup><https://github.com/spacetelescope/calcos>

<sup>4</sup><https://extinction.readthedocs.io/>

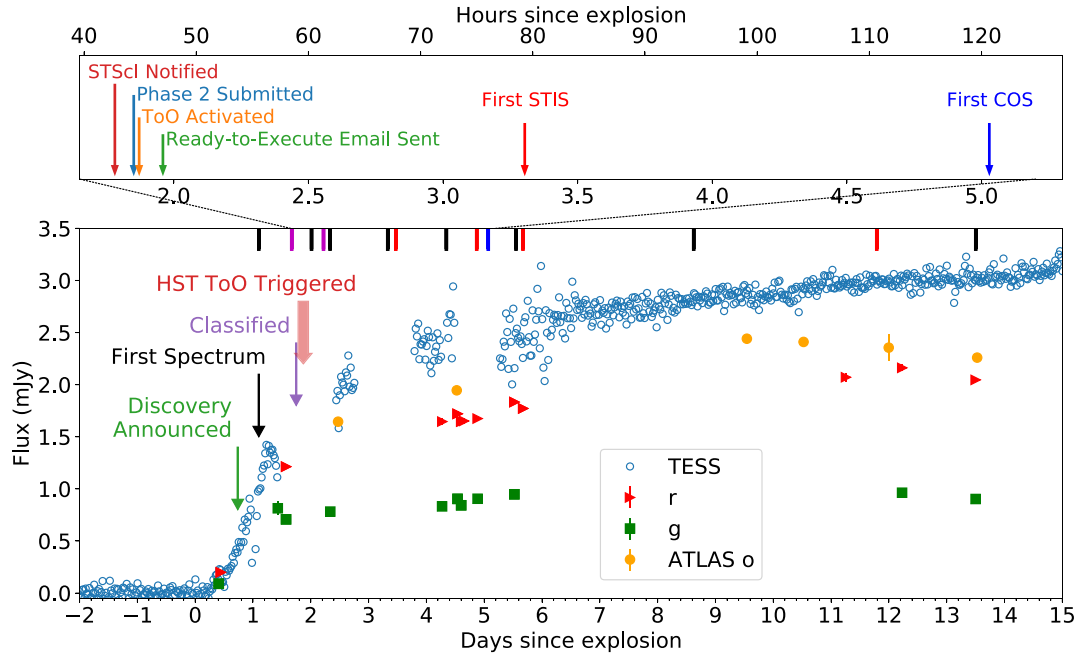


**Figure 2.** Early photometry of SN 2020fqv from *TESS*, along with select early ground-based photometric observations. We mark the timeline of the events, including the discovery announcement at 2020 March 31, 15:59 (18 h post-explosion); our first spectrum at 2020 April 01, 00:44 (26 h post-explosion); classification on TNS at 2020 April 01, 16:16 (42 h post-explosion; Zhang et al. 2020); and our *HST* ToO trigger at 2020 April 01, 21:21, which leads to the first *HST* STIS spectrum obtained at 2020 April 03, 05:36, 79 h after the explosion. Black ticks on the top of the bottom panel mark epochs of ground-based spectra in this work; red ticks are STIS spectra; and the blue tick is the one epoch of COS observations. Magenta ticks mark the epochs of the public spectra available on TNS for this object. The width of the arrow marked ‘*HST* ToO Triggered’ in the main plot corresponds to the time span between ‘STScI Notified’ to ‘Ready-to-Execute Email Sent’ in the top inset.

**Table 1.** Log of *HST* observations of SN 2020fqv.

Date	MJD	Epoch (day)	Instrument/Detector	Grating	Exp. Time (s)
2020-04-03	58942.31	3.38	STIS/CCD	G230LB	6297
2020-04-03	58942.45	3.52	STIS/CCD	G430L	920
2020-04-04	58943.89	4.96	STIS/NUV	G230L	964
2020-04-04	58943.74	4.81	STIS/CCD	G430L	1788
2020-04-04	58943.96	5.03	COS/FUV	G160M	2032
2020-04-05	58944.02	5.09	COS/FUV	G130M	5120
2020-04-05	58944.54	5.61	STIS/CCD	G230LB	5089
2020-04-05	58944.64	5.71	STIS/CCD	G430L	920
2020-04-11	58950.71	11.8	STIS/NUV	G230L	964
2020-04-11	58950.73	11.8	STIS/CCD	G430L	868
2020-04-17	58956.69	17.8	STIS/NUV	G230L	5215
2020-04-17	58956.81	17.9	STIS/CCD	G430L	1702

Note. STIS/NUV refers to the NUV-MAMA detector

### 2.3 *TESS* photometry

SN 2020fqv occurred within camera 1 CCD 3 of *TESS* during sector 23 which observed at 30 min cadence from 58928 to 58954 MJD. The rise of SN 2020fqv coincided with the end of orbit 53 and the start of orbit 54, during which time camera 1 suffered from extreme levels of scattered light from the Earth and Moon.<sup>5</sup> This extreme background led to detector saturation and data loss in camera 1 in the following two periods: 58941.68 to 58942.73 MJD and 58943.41 to 58944.20 MJD.

<sup>5</sup>[https://archive.stsci.edu/missions/tess/doc/tess\\_drn/tess\\_sector\\_23\\_drn32\\_v03.pdf](https://archive.stsci.edu/missions/tess/doc/tess_drn/tess_sector_23_drn32_v03.pdf)

Reducing *TESS* data for SN 2020fqv was further complicated by the source falling on columns that contain a feature of the detector known as a ‘strap’. As described in the *TESS* handbook<sup>6</sup> the straps scatter IR light that initially passes through the detector back into the detector, this has a colour-dependent effect of enhancing the quantum efficiency of strap columns and neighbouring columns. This complex background feature, alongside the extreme levels of scattered light, which can be seen in Fig. 4, at the rise of SN 2020fqv presented a substantial challenge to extracting a clean *TESS* light curve.

To address these challenging data, we developed a data reduction pipeline for *TESS* that reliably determines the background. This pipeline, known as *TESSreduce*, is publicly available on GitHub.<sup>7</sup> While other *TESS* difference imaging pipelines such as those presented in Valley et al. (2021), Bouma et al. (2019) and Woods et al. (2021) can produce a smoothed background, they fail to correctly account for the straps. Since SN 2020fqv lies close to prominent straps, we developed the following pipeline to correct for both the smooth background as well as the strap background.

To determine the complex *TESS* background we first mask all-known sources. We query the *Gaia* and PS1 source catalogues through CASJobs to a depth of 19th magnitude and for each source scale the mask according to the *G*-band magnitude for *Gaia*, and *i*-band magnitude for PS1. The limit of 19th magnitude is chosen, as it is close to the *TESS* detection limit, while still allowing enough pixels for background determination. We also mask all known transients in the image, such as SN 2020fqv. Since

<sup>6</sup>[https://archive.stsci.edu/files/live/sites/mast/files/home/missions-and-data/active-missions/tess/\\_documents/TESS\\_Instrument\\_Handbook\\_v0.1.pdf](https://archive.stsci.edu/files/live/sites/mast/files/home/missions-and-data/active-missions/tess/_documents/TESS_Instrument_Handbook_v0.1.pdf)

<sup>7</sup><https://github.com/CheerfulUser/TESSreduce>

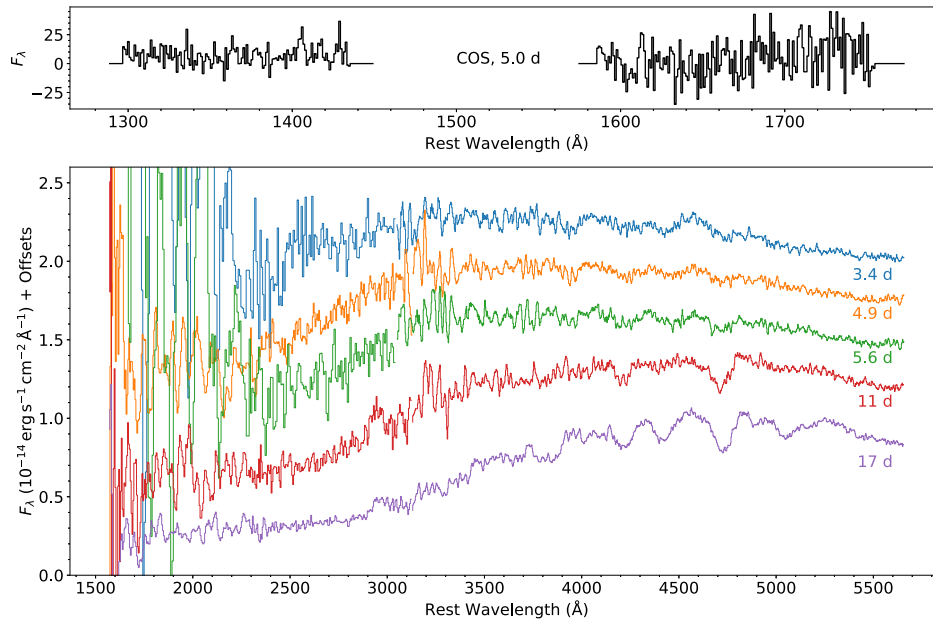


**Figure 3.** COS (top panel) and STIS (bottom panel) spectra of SN 2020fqv from 3 to 17 d post-explosion. Fluxes in both panels are in the same units. COS spectra were taken at 5 d post-explosion with the G130M and G160M gratings in the FUV mode. There was no detection. For STIS, all the red channel data were taken using the CCD and the G430L grating. The blue channel data on days 3.4 and 5.6 were taken with the CCD and the G230LB grating, the rest were taken with the NUV-MAMA detector and the G230L grating. The spectra were corrected for dust extinction using the parameters derived in Section 3.1. The red ( $\lambda \gtrsim 3000 \text{ \AA}$ ) part of the spectra and the blue MAMA data were binned by 3 pixels and the blue CCD data were binned by 5 pixels to improve the S/N. The uncorrected spectra are available via WISREPEP.

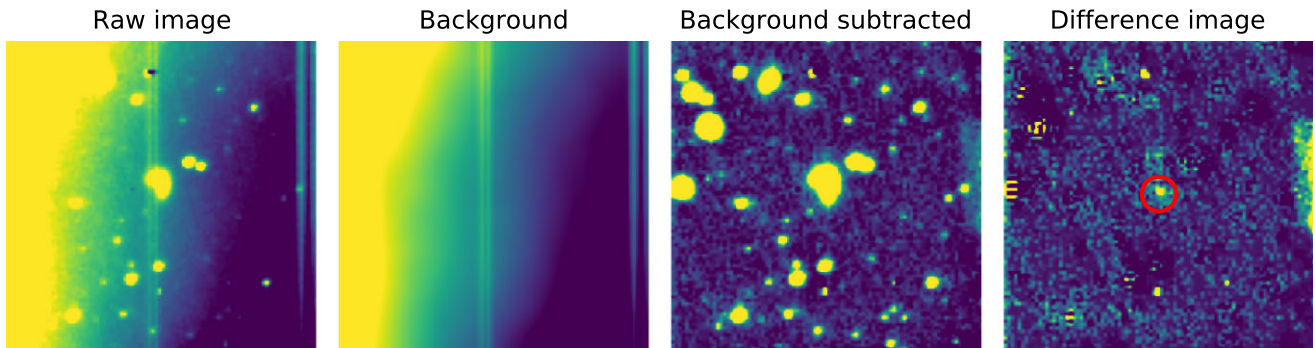


**Figure 4.** Reduction stages for a high background *TESS*  $90 \times 90$  pixel ( $31 \text{ arcmin} \times 31 \text{ arcmin}$ ) image cut-out centred on SN 2020fqv. The presence of extreme scattered light, detector straps and a spatially varying host requires a precise reduction method. The leftmost panel shows the raw image from *TESS*. The centre left-hand panel shows the instrument background model including the scattered light and the detector strap. The centre right panel shows the sky image after background subtraction. The rightmost panel shows the difference image whereby a pre-explosion image is used to subtract the static host galaxy, revealing SN 2020fqv in the red circle.

the source catalogues do not contain accurate galaxy morphology information, we augment the source mask by adding remaining bright pixels to the mask that are identified by sigma clipping the source masked *TESS* image for a low background image. This final mask is taken as the total source mask for all images.

With all sources masked, we break the background determination into two components: a smooth continuous background and a discrete background defined by the detector straps. Alongside the source mask, we also construct a strap mask to mask out the strap columns and include the three neighbouring columns as a buffer zone. To construct the smooth background we mask out the strap regions and for each frame we interpolate the background over all masked pixels using the `SCIPY gridspec` with a linear method. We then smooth

the background using a Gaussian kernel with a standard deviation of 3 pixels.

The strap background is determined by identifying the effective quantum efficiency enhancement that the strap provides in each frame. We identify the enhancement for each column by masking all known sources and then calculate the median of the strap column counts divided by the smooth background which is interpolated over the strap columns. For small regions (e.g.  $90 \times 90$  pixels), or times with little scattered light the scaling factor is constant for each column. To get the full background we multiply the strap scaling, as seen in Fig. 4, with the smooth background. This background is largely free of biases from sources and artefacts like straps, allowing us to reliably subtract the extreme background present in sector 23 camera 1 of *TESS* data.

**Table 2.** Observed ATLAS and synthetic *TESS* magnitudes used for photometric calibration.

MJD	ATLAS <i>o</i> (mag)	<i>TESS</i> (syn-mag)
58941.26	15.86	15.66
58943.28	15.68	15.48

Another crucial component to reduce *TESS* data for SN 2020fqv is to account for any pointing drift. Although *TESS* has excellent temporal resolution, it has coarse spatial resolution with 21 arcsec pixels. Even with *TESS*'s relatively stable pointing, for spatially complex targets like NGC 4568, small shifts of 0.01 pixels can lead to substantial changes to the counts contained in an aperture. For each image we identify the shift relative to a low background reference image using the `PHOTUTILS DAOSTarFinder` routine (Bradley et al. 2020), the images are then aligned using the `SCIPY ndimage shift` routine (Virtanen et al. 2020). This alignment procedure reduces signals produced by telescope motion, allowing for effective difference imaging.

Following the background subtraction and image alignment we calculate flux through standard aperture photometry. We use a  $3 \times 3$  pixel source aperture and an annulus sky aperture, the resulting light curve is in un-calibrated *TESS* counts. The calibration of *TESS* counts to physical units is presented in Section 2.4.

## 2.4 *TESS* photometric calibration

*TESS* features a broad-band red filter that covers a wavelength range of 5802.57 to 11171.45 Å. We calibrate the SN 2020fqv *TESS* light curve using synthetic photometry to the FLOYDS spectra taken during the rise which covers a wavelength range of 3200 to 10000 Å. Since the FLOYDS spectra does not completely cover the *TESS* bandpass, we extrapolate the spectra to 11 500 Å, using blackbody spectrum fit to each spectra. Furthermore, we smooth the original spectra using the `SCIPY Savitzky-Golay` filter, with a window length of 21 wavelength bins and a third order polynomial. Although there is considerable uncertainty in the extrapolated region, the range we extrapolate over coincides with the decline to the red cut-off of the *TESS* bandpass, reducing the overall impact.

We flux calibrate the FLOYDS spectra to coincidental *o* band observations from ATLAS. We use FLOYDS spectra taken at 58941.26 MJD and 58943.28 MJD since they have ATLAS observations within 0.2 d, limiting the evolution that occurs between the data. We calculate the synthetic magnitude of the ATLAS *o* band for both spectra and normalize the spectrum such that the synthetic spectra equal the observed. Using the flux calibrated FLOYDS spectra, we calculate the synthetic *TESS* magnitude using the *TESS* bandpass available on SVO (Rodrigo, Solano & Bayo 2012; Rodrigo & Solano 2020) and algorithms in the `PYSYNPHOT` package (STScI Development Team 2013). The FLOYDS spectra used, alongside the *TESS* and ATLAS *o* bandpasses are shown in Fig. A1.

Finally the zero-point is calculated by comparing the synthetic magnitudes, shown in Table 2, to the 6 hour averaged *TESS* light curve. We find an AB zero-point of  $zp = 20.81 \pm 0.02$ . Fig. 2 shows the final *TESS* photometry, along with our early observational timeline.

## 2.5 Ground-based photometry

SN 2020fqv was well observed in the *griz* bands with the Panoramic Survey Telescope and Rapid Response System (Pan-STARRS) at

Haleakalā Observatory in Hawai'i, as part of YSE. In addition, we obtained optical photometry from the Las Cumbres Observatory network (Brown et al. 2013a), Thacher Observatory (Swift et al. in preparation), Lulin Observatory, and the Nickel telescope at Lick Observatory. The optical photometry was processed in the way explained in Kilpatrick et al. (2018) using `photpipe` (Rest et al. 2005). We retrieved public photometry of this SN from ATLAS and ZTF (Bellm et al. 2019; Masci et al. 2019). We also obtained near-IR photometry in the *J*-band, using the 0.3-m Gattini-IR telescope at Palomar Observatory (Moore & Kasliwal 2019; De et al. 2020). Fig. 5 shows the light curves of SN 2020fqv, uncorrected for reddening, along with the interpolated light curves discussed in Section 3.3.

## 2.6 Swift photometry

The Neil Gehrels *Swift* Observatory obtained imaging of SN 2020fqv with the Ultraviolet/Optical Telescope (UVOT; Roming et al. 2005) from 2020 April 1 to 2020 May 29. We downloaded these imaging from the calibrated sky frames from the *Swift* data archive and performed forced aperture photometry at the site of SN 2020fqv as determined by aligning the *Swift* frames to our Pan-STARRS photometry of the transient described above. We used `HEASOFT v6.27.2` (Nasa High Energy Astrophysics Science Archive Research Center (Heasarc) 2014) to perform this analysis with the UVOT aperture photometry method `uvot_source` and an aperture radius of 3 arcsec and background radius of 30 arcsec. All aperture photometry was calibrated using the latest *Swift*/UVOT calibration files for `HEASOFT`.

## 2.7 Ground-based optical spectroscopy

We obtained 20 spectra of SN 2020fqv ranging from 1 to 373 d post-explosion, well sampling the plateau phase with three epochs in the nebular phase. Table 3 summarizes the observations, providing the epoch of observation, telescope and instrument, and exposure time. Spectra presented here were obtained using the SPECTROGRAPH for the Rapid Acquisition of Transients (SPRAT; Piascik et al. 2014) on the Liverpool Telescope (LT); FLOYDS on the 2-m telescopes of Las Cumbres Observatory (LCO) at Haleakalā Observatory in Hawai'i and Siding Spring Observatory in Australia (Brown et al. 2013b); Kast Double Spectrograph (Miller & Stone 1993) on the 3-m Shane telescope at Lick Observatory in California; Gemini Multi-Object Spectrograph (GMOS; Hook et al. 2004) on the Gemini North Telescope on Maunakea in Hawai'i; and the Low-resolution Imaging Spectrograph (LRIS; Oke et al. 1995) on the Keck Telescope, also atop Maunakea. Spectra were reduced and extracted using standard data reduction pipelines for the respective instruments.

Six optical spectra were obtained with the GMOS instrument under program GN-2020A-Q-134 (PI: Foley). We used the long-slit spectroscopy mode, with the 0.75 arcsec slit width and the B600 + R400 gratings (wavelength range of 4000–9800 Å). The spectra were reduced, extracted, and calibrated using the `IRAF gemini` package, with the reduction steps described at the GMOS Data Reduction Cookbook.<sup>8</sup>

Shane/Kast and Keck/LRIS spectra were reduced using our customized data reduction pipeline.<sup>9</sup> It performs the standard field flattening, spectral extraction, wavelength calibration using arc observations, and flux calibration using observations of standard stars

<sup>8</sup>[http://ast.noao.edu/sites/default/files/GMOS\\_Cookbook/](http://ast.noao.edu/sites/default/files/GMOS_Cookbook/)

<sup>9</sup>[https://github.com/msiebert1/UCSC\\_spectral\\_pipeline](https://github.com/msiebert1/UCSC_spectral_pipeline)

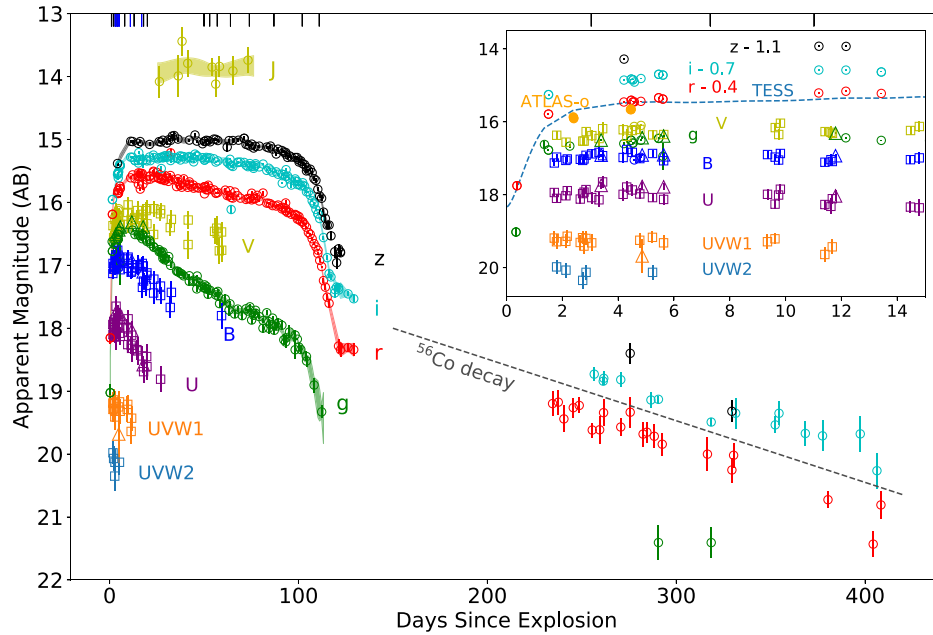


**Figure 5.** Photometry of SN 2020fqv in the *UVW1*, *UVW2*, and *UVBgrizJ* bands. Circles are ground-based photometry; squares are photometry from *Swift*; triangles are synthetic photometry from *HST/STIS* spectra. Shaded regions during the plateau phase show the light curve interpolation for the *grizJ* bands as described in Section 3.3. The inset shows early-time photometry, up to 15 d post-explosion, with ATLAS *o*-band photometry included (filled circles). The dotted line in the inset is the smoothed, interpolated *TESS* light curve. The photometry is not corrected for reddening; no offsets are applied except for the *riz* bands in the inset. The offsets used are provided. Black and blue ticks on the top of the plot mark the epochs of ground-based and *HST* spectroscopy, respectively. The grey dashed line indicates the rate of decline expected from radioactive decay of  $^{56}\text{Co}$  in the nebular phase.

**Table 3.** Log of ground-based spectroscopic observations.

Date	MJD	Epoch (d)	Telescope/Instrument	Exp. Time (s)
2020-04-01	58940.03	1.1	LT/SPRAT	900
2020-04-01	58940.94	2.0	LT/SPRAT	600
2020-04-02	58941.3	2.3	LCO/FLOYDS	900
2020-04-03	58942.3	3.3	LCO/FLOYDS	900
2020-04-04	58943.3	4.3	LCO/FLOYDS	1800
2020-04-08	58947.6	8.6	LCO/FLOYDS	1500
2020-04-13	58952	13	LCO/FLOYDS	1500
2020-04-18	58957	18	LCO/FLOYDS	1500
2020-04-19	58959	20	LT/SPRAT	600
2020-05-20	58989	50	Gemini/GMOS	900
2020-05-23	58992	53	Shane/Kast	900
2020-05-27	58996	57	Shane/Kast	930
2020-06-03	59003	64	Gemini/GMOS	900
2020-06-13	59013	74	Gemini/GMOS	900
2020-06-26	59026	84	Gemini/GMOS	900
2020-07-11	59041	102	Gemini/GMOS	900
2020-07-20	59050	111	Gemini/GMOS	1200
2020-12-11	59194	255	Keck/LRIS	1800
2021-02-12	59257	318	Keck/LRIS	1200
2021-04-08	59312	373	Keck/LRIS	1500

taken the same night. A similar procedure was used for the reduction of the LCO/FLOYDS spectra with the pipeline described in Valenti et al. (2014).

SPRAT spectra were obtained in good seeing (1–1.2 arcsec FWHM) conditions. They have a wavelength range of 4000–8000 Å, slit width 1.8 arcsec,  $R = 350$  at the centre of the spectrum, with the grating optimized for the blue throughput. They were reduced and

extracted using the SPRAT data reduction pipeline and individual spectra were combined in IRAF with cosmic ray rejection.

Fig. 6 shows the sequence of optical spectra of SN 2020fqv. The Na I D doublet absorption at the host redshift is present in all spectra, and resolved into two lines in GMOS spectra. We measured the equivalent width (EW) of the Na I D 1 and 2 lines to be 1.14 and 2.30, respectively. The EW of the Na I D 1 and 2 lines remain constant throughout the plateau phase. The Na doublets are saturated at this EW, and their strength is no longer a good probe of the interstellar extinction (Poznanski, Prochaska & Bloom 2012). We discuss the determination of dust extinction towards this SN in Section 3.1.

## 2.8 Archival imaging

### 2.8.1 Hubble space telescope

We obtained pre-explosion (*HST*) imaging of NGC 4568 from the Barbara A. Mikulski Archive for Space Telescopes (MAST).<sup>10</sup> These data consisted of a single epoch of F606W imaging obtained with the Wide Field Planetary Camera 2 (WFPC2) from 4 February 1995 (Program 5446, PI: Illingworth), roughly 25 yr before the explosion of SN 2020fqv. This was the only *HST* image covering the SN site. We downloaded the calibrated science frames (c0m) and aligned, masked, drizzled, and performed *DOLPHOT* photometry (Dolphin 2016) using the *hst123* reduction pipeline (Kilpatrick et al. 2021).

We aligned the final drizzled F606W image to a stacked *i*-band frame of SN 2020fqv constructed from our Las Cumbres Observatory

<sup>10</sup><https://archive.stsci.edu/hst/>

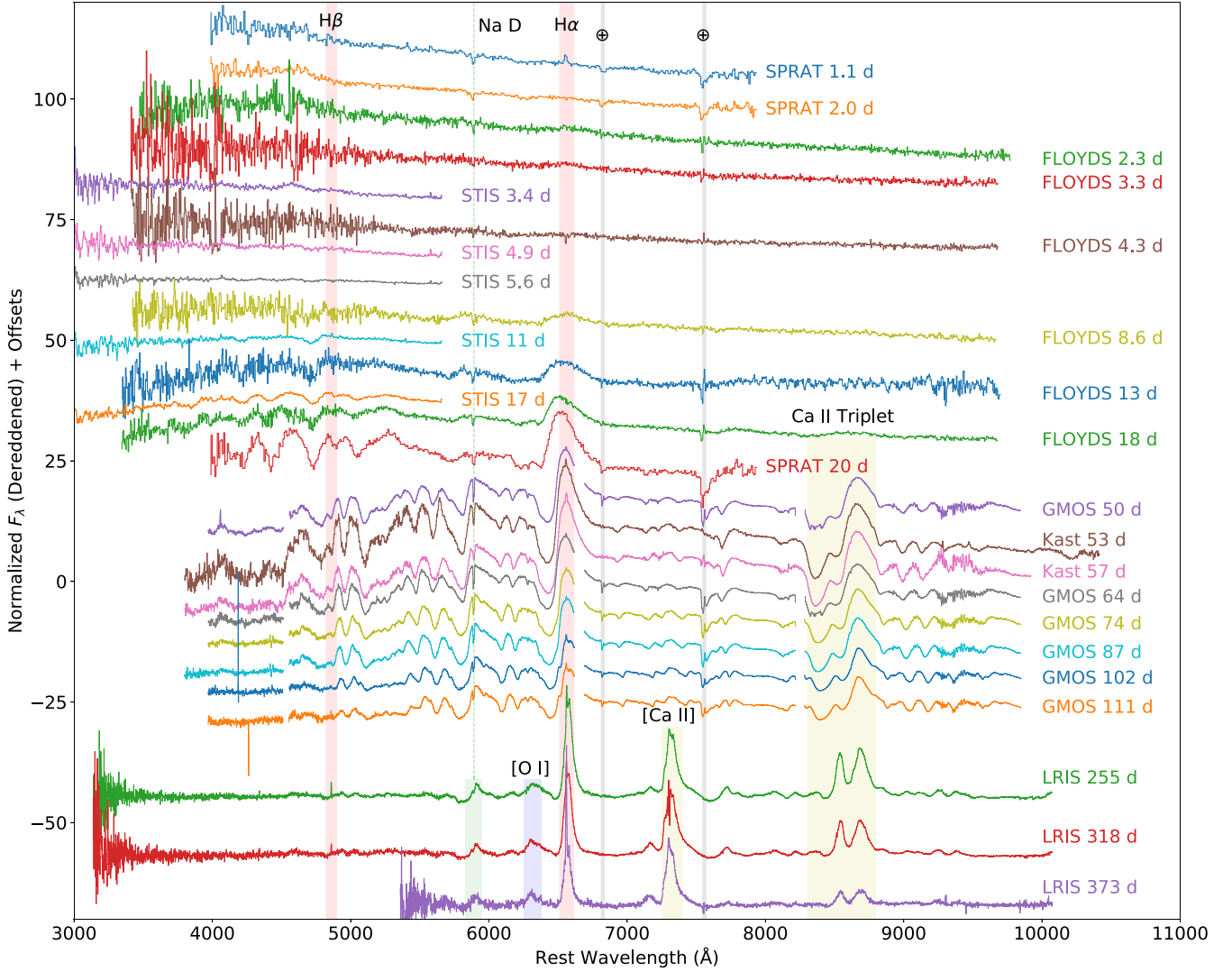


**Figure 6.** Optical spectra of SN 2020fqv ranging from 1 to 318 d post-explosion. Major spectral lines are marked. The H  $\alpha$  in the first spectrum at 1.1 d may be from host. The telluric bands are marked with  $\oplus$  symbols. The spectra are corrected for dust extinction using the parameters derived in Section 3.1. Note that the GMOS spectra have some gaps in the wavelength coverage due to the chip gaps. Also note that the excess flux in the red of the FLOYDS spectrum at 13 d post-explosion with respect to spectra at 8 and 18 d is due to an incomplete galaxy background subtraction. The lack of observations between 18 and 50 d post-explosion is due to the shutdown of observatories worldwide due to COVID-19. The calibrated spectra uncorrected for reddening are available via WISEREP.

**Table 4.** Pre-explosion constraints on optical and infrared counterparts to SN 2020fqv.

Instrument	Band	Epoch (d)	Limiting Magnitude (AB mag)
<i>HST</i> /WFPC2	F606W	−9188	24.80
PS1/GPC1	<i>g</i>	−3697 to −2225	20.80
PS1/GPC1	<i>r</i>	−3692 to −2116	20.36
PS1/GPC1	<i>i</i>	−3689 to −2121	20.48
PS1/GPC1	<i>z</i>	−3949 to −2278	20.32
PS1/GPC1	<i>y</i>	−3718 to −2464	20.05
<i>Spitzer</i> /IRAC	Ch1	−5780 to −158	22.74
<i>Spitzer</i> /IRAC	Ch2	−5780 to −158	23.10

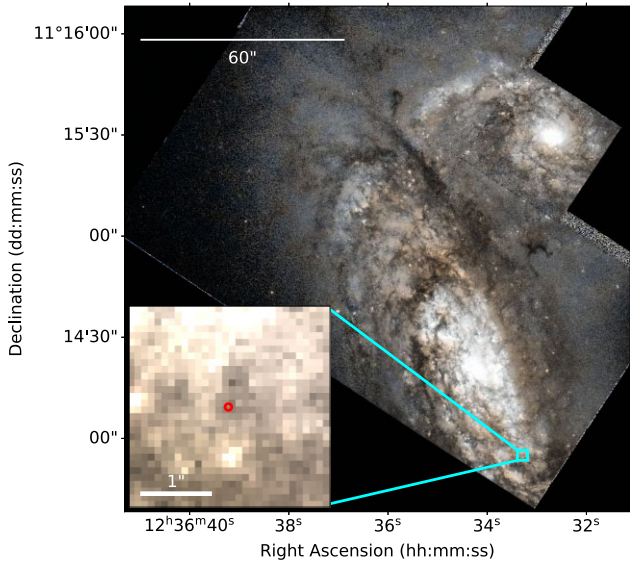
follow-up imaging. Using 5 common astrometric sources, the root-mean square alignment precision was  $\sim 0.05$  arcsec, or roughly 0.5 WFPC2 pixels. Fig. 7 shows the colorized pre-explosion *HST*

image of the SN site with the location of SN 2020fqv marked. There are no sources detected in the WFPC2 image within 6.8 times the astrometric uncertainty. We estimated the limiting magnitude in the image by injecting artificial stars with varying magnitudes at the location of SN 2020fqv with varying magnitudes and recovering them with DOLPHOT. In this way, we estimate the  $3\sigma$  limiting magnitude to be  $m_{F606W} = 24.80$  mag (AB) as reported in Table 4.

### 2.8.2 Spitzer Space Telescope

We downloaded pre-explosion *Spitzer Space Telescope* imaging covering the site of SN 2020fqv from the *Spitzer* Heritage Archive.<sup>11</sup> These consisted of approximately 11 200 s of cumulative exposure in the Infrared Array Camera (IRAC) Channel 1 and 11,100 in Channel

<sup>11</sup><https://sha.ipac.caltech.edu/>



**Figure 7.** Pre-explosion *HST*/WFPC2 image of NGC 4567 (north-west) and 4568 (south-east), containing the site of SN 2020fqv in the F606W filter. The image was taken on 4 Feb 1995 (Program 5446, PI Illingworth). We apply square-root stretch to improve the dynamic range of the image. The monochromatic *HST* image is colorized by using the colour information from the Digitized Sky Survey (DSS). The 3 arcsec  $\times$  5 arcsec area around the SN site is shown in an inset with the SN location marked with the red circle. The size of the circle represents the astrometric uncertainty of 0.05 arcsec (see the text).

2 and spanning 2004 June 22 to 2019 October 31, or 15.8–0.4 yr before explosion of SN 2020fqv. Following procedures described in Jacobson-Galán et al. (2020) and Kilpatrick et al. (2021), we stacked these data using a custom pipeline based on the PHOTPIPE imaging and photometry pipeline (Rest et al. 2005). The frames for each channel were optimally stacked and regridded to a common pixel scale of 0.3 arcsec pixel<sup>-1</sup>. Aligning to our post-explosion imaging, we did not detect any point-like emission at the site of SN 2020fqv, and so injecting artificial stars at this location we recovered limiting magnitudes of 22.74 mag and 23.10 mag on any pre-explosion counterpart to SN 2020fqv in Channels 1 and 2, respectively.

### 2.8.3 Pan-STARRS 3 $\pi$ imaging

We obtained pre-explosion Pan-STARRS imaging in *grizy* bands from the 3 $\pi$  survey (Flewelling et al. 2020). These consisted of stacked frames covering 10.8 to 5.8 yr before the explosion of SN 2020fqv. Processing these data in PHOTPIPE as described in Jones et al. (2021), we did not detect any point-like emission at the site of SN 2020fqv. We derived upper limits on the presence of a counterpart to SN 2020fqv by injecting artificial stars, and we report our 3 $\sigma$  limits in Table 4.

## 3 ANALYSIS

### 3.1 Dust extinction

There is substantial dust extinction in the line of sight towards SN 2020fqv. The lack of the Na I D absorption at  $z = 0$  and the low value of Galactic extinction of  $E(B - V)_{\text{MW}} = 0.029$  mag (Schlafly & Finkbeiner 2011) indicate that the extinction is primarily from the host galaxy. We estimate the dust extinction by assuming that at 4 d post-explosion, the spectrum of the SN is well described by

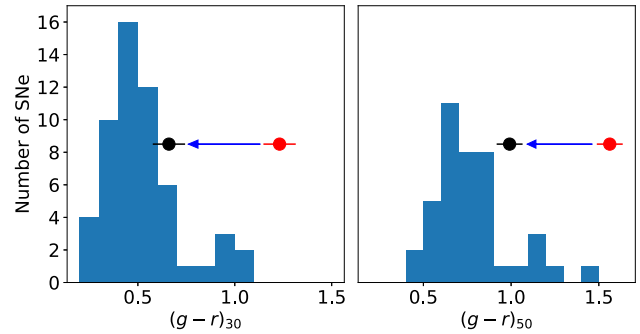


**Figure 8.** Histograms showing the  $g - r$  colour of SNe II from de Jaeger et al. (2018) at 30 (left) and 50 (right) d post-explosion. The colours of SN 2020fqv before and after the extinction correction are plotted in red and black, respectively, in each plot. This demonstrates that after the extinction correction derived from early-time spectroscopy, the colour of SN 2020fqv is similar to that of other SNe II.

a blackbody. We then fit the *HST* and ground-based spectra from 4 d with a blackbody model, leaving the temperature, blackbody radius, and the dust extinction parameters  $E(B - V)$  and  $R_V$  as free parameters. The extinction law used is Fitzpatrick (1999). The fit is performed using the Markov chain Monte Carlo (MCMC) package EMCEE (Foreman-Mackey et al. 2013a). The prior distribution for all parameters is uniform for values that are physical (e.g. positive temperature and radius). The best-fitting extinction parameters are  $E(B - V) = 0.52 \pm 0.01$  mag and  $R_V = 3.19 \pm 0.04$ . Fig. A3 shows the result of this fit. We use these extinction corrections for all subsequent analyses.

To check that the reddening correction is reasonable, we compare the  $g - r$  colour of SN 2020fqv at 30 and 50 d post-explosion,  $(g - r)_{30, 50}$ , with a sample of SNe II from de Jaeger et al. (2018). Fig. 8 shows histograms of the  $g - r$  colours at 30 and 50 d post-explosion from de Jaeger et al. (2018), and the colours of SN 2020fqv before and after the correction. Before we correct for the dust reddening from the host galaxy, the observed colours of SN 2020fqv are  $(g - r)_{30, \text{obs}} = 1.23 \pm 0.08$  mag and  $(g - r)_{50, \text{obs}} = 1.56 \pm 0.07$  mag, well outside of the colour distribution of SNe II in de Jaeger et al. (2018) (figs A3 and A4 in their paper). With our inferred dust reddening parameter, the  $g - r$  colour correction is 0.57 mag, which brings the colours down to  $(g - r)_{30} = 0.66 \pm 0.08$  mag and  $(g - r)_{50} = 0.99 \pm 0.07$  mag. These colours are consistent with other SNe II in the sample.

### 3.2 Time of explosion

With early *TESS*, *ATLAS*, and ZTF  $g$  and  $r$  photometry, we can determine the explosion time by fitting analytical CCSNe rise models. We fit the RSG model, without shock breakout, from Nakar & Sari (2010) following Garnavich et al. (2016) and Vallely et al. (2021). We set the progenitor mass to be  $15 M_{\odot}$ , allowing progenitor radius, explosion energy and explosion time to be free parameters. We will show how we derive this mass estimate from light curve fitting (Sections 3.4.1 and 3.4.2) and nebular spectroscopy (Section 3.4.3). Since the Nakar models assume blackbody emission, we apply the extinction derived in Section 3.1 to the blackbody spectrum using the extinction law of Fitzpatrick (1999). Magnitudes are then calculated by applying the *TESS*, *ATLAS*  $o$ , and ZTF bandpasses to the spectrum and integrating over it at each time-step.

We simultaneously fit all free parameters to *TESS*, *ATLAS*, and ZTF photometry before MJD = 58957 using emcee (Foreman-

Mackey et al. 2013b). We use flat priors for all variables and maximize  $-\chi^2$  in flux space. The best fit parameters, shown in Fig. A2, are  $R = 120_{-30}^{+40} R_{\odot}$ ,  $E = 0.77_{-0.15}^{+0.17} \times 10^{51}$  erg, and explosion time of  $t_0 = 58938.93_{-0.16}^{+0.15}$  MJD, where  $R$  and  $E$  are the progenitor radius and the explosion energy, respectively. We note that these values are different from those presented in Vallely et al. (2021) for SN 2020fqv; however, there are a few key differences. For example, we use a photometric zeropoint calibrated to concurrent spectra and photometry, this will lead to different peak fluxes. Furthermore, while Vallely et al. (2021) fit to an analytical model, we fit the semi-analytic Nakar & Sari (2010) model simultaneously to multiple bands. We also note that the radius is small for a RSG, but this is because the model does not take CSM interaction into account.

Although we constrain progenitor properties with this model, aside from explosion time, they are unreliable. As can be seen in Fig. A2, the best-fitting model cannot match the rapid rise of the SN 2020fqv light curves in all bands, likely due to ejecta interacting with a dense circumstellar medium. Despite the shortcomings, this model provides us with a self-consistent and physically motivated way to extrapolate all light curves to early times. While, the fit fails to produce realistic parameters for the progenitor radius, it does agree well with early observations in all bands until  $\sim 58940$  MJD. Therefore, we only use the explosion time from this fit, and model progenitor properties in Section 3.4.

### 3.3 Quasi-bolometric luminosity

To estimate the total radiative energy, we compute the quasi-bolometric luminosity of SN 2020fqv using the following steps. First, the photometric data in different bands are generally taken at different epochs, so we interpolate them on to a common time grid. We only perform this interpolation for the data during the plateau phase. We use the Gaussian process regression package `GEORGE` to perform the interpolation (Ambikasaran et al. 2015). We use the Matérn 3/2 kernel, which is less likely to smooth out features of the light curve compared to the more commonly used exponential squared kernel as suggested in Boone (2019). The length-scale parameter used for the Gaussian process was 200 d. We find no significant difference between using the two kernels. We also find no difference in results between interpolating each band at a time and interpolating all bands simultaneously, assuming that the evolution in one band resembled that in the adjacent bands. We do not extrapolate the data more than two days from the actual observation. The interpolation is performed in the flux space. Along with the photometry, Fig. 5 shows the interpolated light curves in each band.

For each epoch, we fit the multiband photometry with a blackbody model reddened by the dust extinction model discussed in Section 3.1. For epochs with more than two bands available, we do not fit the  $r$  band to avoid the significant  $H\alpha$  line. Fig. 9 shows the resulting luminosity, temperature, and black-body radius. The error bars in the plot represent statistical errors due to photometric uncertainties. The shaded bands represent systematic errors due to the uncertainty in the extinction correction and the distance to the SN. Note that for the luminosity and radius, the distance uncertainty dominates the overall uncertainty; for the temperature, only the extinction uncertainty contributes to the systematics.

### 3.4 Progenitor mass and explosion properties

We estimate the explosion properties of SN 2020fqv, which are the explosion energy, progenitor mass, and  $^{56}\text{Ni}$  mass, using four independent methods.

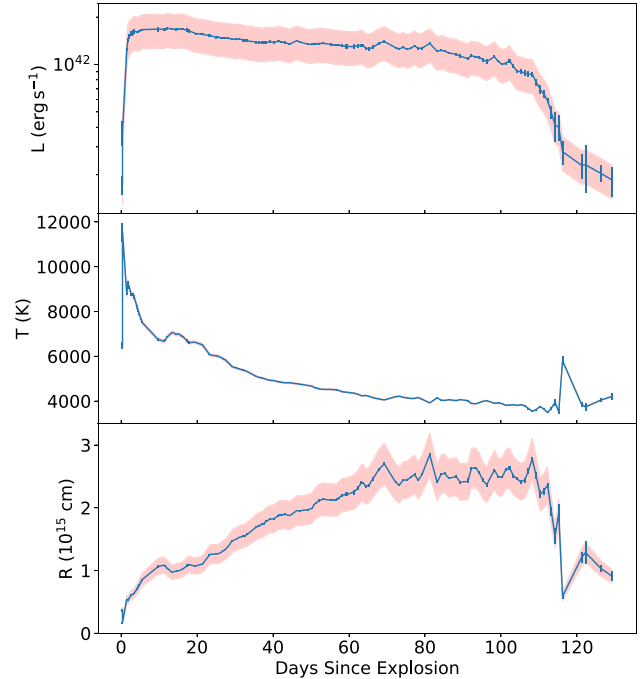


**Figure 9.** Results of fitting a blackbody model to the multiband light curves of SN 2020fqv. From top to bottom: quasi-bolometric luminosity, blackbody temperature, and blackbody radius. For each of the blackbody parameters, error bars represent  $1\sigma$  statistical uncertainty due to photometric uncertainties; shaded bands represent the systematic uncertainty from the extinction correction and the distance to the SN. For the luminosity and blackbody radius, the systematic uncertainty is dominated by the distance uncertainty. For the temperature, only the uncertainty in the extinction correction contributes to the systematic uncertainty.

#### 3.4.1 Scaling relations derived from models

First, we obtain estimates of the explosion properties by using scaling relations from Sukhbold et al. (2016), which are derived using results from the KEPLER SN explosion models. Equations (15) and (19) from Sukhbold et al. (2016) relate the explosion energy, hydrogen envelope mass, and progenitor radius to the observed parameters: luminosity at 50 d ( $L_{50}$ ), plateau length ( $t_p$ ), and the amount of  $^{56}\text{Ni}$  synthesized ( $M_{\text{Ni}}$ ). The luminosity at 50 d can be obtained directly from our quasi-bolometric light curve described in the last section:  $L_{50} = (1.3 \pm 0.3) \times 10^{42} \text{ erg s}^{-1}$ . To measure the plateau length, we follow Valenti et al. (2016) and fit their equation (1) to the light curve around the transition between the plateau and the nebular phase; we find the plateau length of  $114 \pm 1$  d. We measure the amount of  $^{56}\text{Ni}$  synthesized in SN 2020fqv by measuring its luminosity in the radioactive decay tail. The only epoch where multiband photometry exists for this purpose is at 270 d post-explosion. At that epoch, SN 2020fqv's luminosity from photometry is  $(5.6 \pm 2.1) \times 10^{40} \text{ erg s}^{-1}$  (the uncertainty includes both uncertainties from photometry and the distance to the SN). Because the decline rate in this phase follows what is expected from radioactive decay of  $^{56}\text{Co}$ , it is reasonable to assume that gamma-ray from radioactivity is efficiently absorbed and re-emitted in the optical. With this assumption, the luminosity of the SN reflects the heating rate from the radioactive decay of  $^{56}\text{Co}$  at the time, and we can compute the amount of  $^{56}\text{Co}$  present at that epoch:  $M_{\text{Co}}(270 \text{ d}) = L(270 \text{ d})/\epsilon_{\text{Co}}$  where  $\epsilon_{\text{Co}} = 6.8 \times 10^9 \text{ erg s}^{-1} \text{ g}^{-1}$  is the heating rate

from the  $^{56}\text{Co}$  decay. Then the  $^{56}\text{Ni}$  mass synthesized (at  $t = 0$ ) is

$$M_{\text{Ni}} = M_{\text{Co}}(t) \frac{\lambda_{\text{Co}} - \lambda_{\text{Ni}}}{\lambda_{\text{Ni}}} [\exp(-\lambda_{\text{Ni}}t) - \exp(-\lambda_{\text{Co}}t)]^{-1}, \quad (1)$$

where  $\lambda_{\text{Ni}}$ ,  $\lambda_{\text{Co}}$  are the inverse of the radioactive decay time-scale of  $^{56}\text{Ni}$  and  $^{56}\text{Co}$ , respectively. With this calculation, we infer  $0.043 \pm 0.017 M_{\odot}$  of  $^{56}\text{Ni}$  synthesized in SN 2020fqv. To double check, we also compare the luminosity of SN 2020fqv to that of SN 1987A, which is known to produce  $0.075 M_{\odot}$  of  $^{56}\text{Ni}$  following e.g. Spiro et al. (2014). At 270 d post-explosion,  $L_{87A} = 9.0 \times 10^{40} \text{ erg s}^{-1}$  (Arnett et al. 1989), and we arrive at  $M_{\text{Ni}} \approx 0.047 M_{\odot}$  for SN 2020fqv, consistent with the first calculation. We adopt  $0.043 M_{\odot}$  as the mass of  $^{56}\text{Ni}$  synthesized in SN 2020fqv.

Lastly, to break the degeneracy between the hydrogen envelope mass and the progenitor radius, we consider the values listed in table 2 in Sukhbold et al. (2016) where  $M_i$  is the initial mass,  $M_f - M_{\alpha}$  is the envelope mass, and  $R_f$  is the progenitor radius. The relationship between  $M_f - M_{\alpha}$  and  $R_f$  is monotonic for  $M_i < 20 M_{\odot}$ , so we only use the values from this range. Other methods discussed later show that this assumption is reasonable.

With these quantities determined, we solve the aforementioned equations (15) and (19) from Sukhbold et al. (2016), using the `fsolve` function in the `SCIPY.OPTIMIZE` package. We arrive at the explosion energy and progenitor mass of  $(4.1 \pm 0.1) \times 10^{50} \text{ erg}$  and  $15 \pm 3 M_{\odot}$ , respectively. For these values, the progenitor radius and the hydrogen envelope mass are  $800 \pm 100 R_{\odot}$  and  $8.5 \pm 0.7 M_{\odot}$ , respectively.

### 3.4.2 Comparison with numerical models

In order to independently confirm the explosion parameters, we compared our observations with a grid of models generated using the SuperNova Explosion Code (SNEC; Morozova et al. 2015) for SN 2004et, which produced a similar amount of  $^{56}\text{Ni}$  (Morozova et al. 2018). These models do not account for CSM interactions. Fig. 10 (top) shows the heat map of the goodness-of-fit figure for the models with different kinetic energies and progenitor masses, showing that the best-fitting values are  $E = (5.5 \pm 0.7) \times 10^{50} \text{ erg}$  and  $M_{\text{ZAMS}} = 16.5 \pm 1.5 M_{\odot}$ , respectively. These numbers are roughly consistent with what we derived from scaling relations in Section 3.4.1. Fig. 10 (bottom) shows the best-fitting light curve on top of the quasi-bolometric luminosity from Fig. 9. We note that at early time prior to 35 d post-explosion, the model substantially underpredicts the luminosity. In the next section, we perform a similar fit accounting for the extra flux from CSM interaction to fully explain the light curve. One consequence from the CSM interaction is that it prolongs the plateau. As such, the progenitor mass required to explain the plateau mass is smaller compared with the CSM-free models used in this section by about  $1.5 M_{\odot}$ . Thus, the range of  $M_{\text{ZAMS}}$  from this method is  $15 \pm 1.5 M_{\odot}$ .

### 3.4.3 Late-time nebular spectroscopy

As an independent measure of the progenitor mass of SN 2020fqv, we compare the nebular phase spectra obtained at 255, 318, and 373 d post-explosion with models from Jerkstrand et al. (2014) ( $12 - 25 M_{\odot}$ ; high mass) and Jerkstrand et al. (2018) ( $9 M_{\odot}$ , low mass). Similar approach has been used in the literature to constrain the progenitor mass of SNe II (e.g. Terreran et al. 2016; Silverman et al. 2017; Bostroem et al. 2019; Szalai et al. 2019; Van Dyk et al. 2019; Hiramatsu et al. 2021). The high-mass models in Jerkstrand et al.

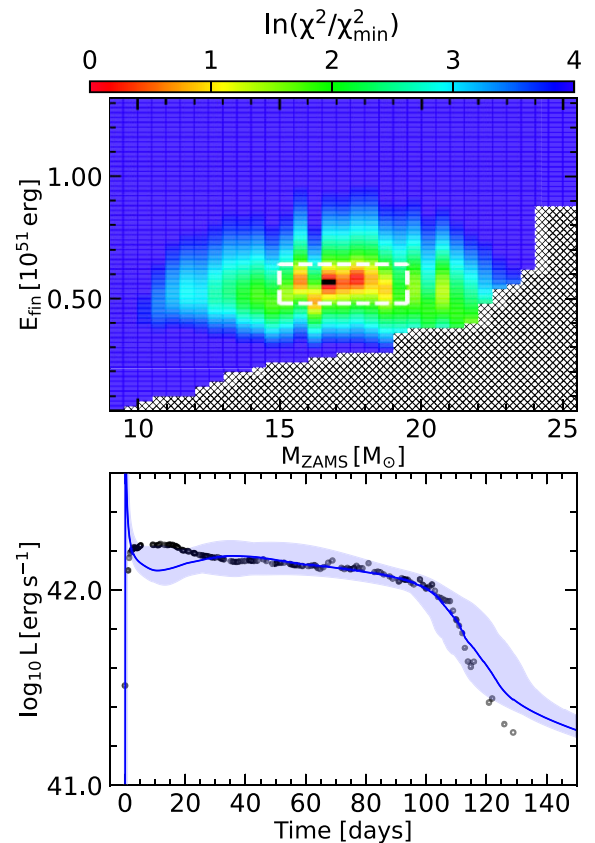


**Figure 10.** Top: A heat map of the goodness-of-fit figure  $\ln(\chi^2/\chi_{\min}^2)$  of different SNEC models compared to the data as a function of the zero-age main sequence mass (ZAMS) of the progenitor star and the kinetic energy of the explosion. The hatched region indicates the parameters for which we could not obtain theoretical light curves because of fallback material. The result shows that the best-fitting explosion parameters of SN 2020fqv are  $M_{\text{ZAMS}} = 16.5 \pm 1.5 M_{\odot}$  and  $E = 5.5 \pm 0.7 \times 10^{50} \text{ erg}$ . This uncertainty box is indicated as a white box in the top panel. These parameters are in rough agreement with the values we derived from simple scaling relation. Bottom: The best-fitting model of the bolometric luminosity of SN 2020fqv. Note that the CSM-less model underpredicts the luminosity less than 1 month post-explosion. The shaded region represents the models from the uncertainty box in the top panel.

(2014) were computed for SN 2012aw at a distance of 5.5 Mpc and with a  $^{56}\text{Ni}$  mass of  $0.062 M_{\odot}$ . The low-mass models in Jerkstrand et al. (2018) were computed for a SN from a  $9 M_{\odot}$  progenitor star at a distance of 10 Mpc with a  $^{56}\text{Ni}$  mass of  $0.0062 M_{\odot}$ . We scale the flux proportionally with the  $^{56}\text{Ni}$  mass and inverse proportionally with distance squared. We note that for the  $9 M_{\odot}$  models, the scaling factor due to the  $^{56}\text{Ni}$  mass is  $\sim 70$ . The closest epochs to the data for which high-mass models are available are 250, 306, and 369 d (for the second epoch, the closest  $19 M_{\odot}$  model available is at 332 d; for the third epoch, the closest  $12 M_{\odot}$  model available is at 400 d). The closest epochs to the data for which low-mass models are available are 200, 300, and 400 d. To account for these differences in epoch, we scale the flux with a factor of  $\exp(x/111.3)$  where  $x$  is the difference between the epoch of the model and the data in days and 111.3 is the lifetime of the  $^{56}\text{Co}$  decay. For instance, for the data at 255 d, the models for 250 d are scaled by a factor of  $\exp(-5/111.3)$ .

The data must be flux calibrated to be compared to the model. To do so, we compute synthetic photometry of the spectra in the  $r$  band

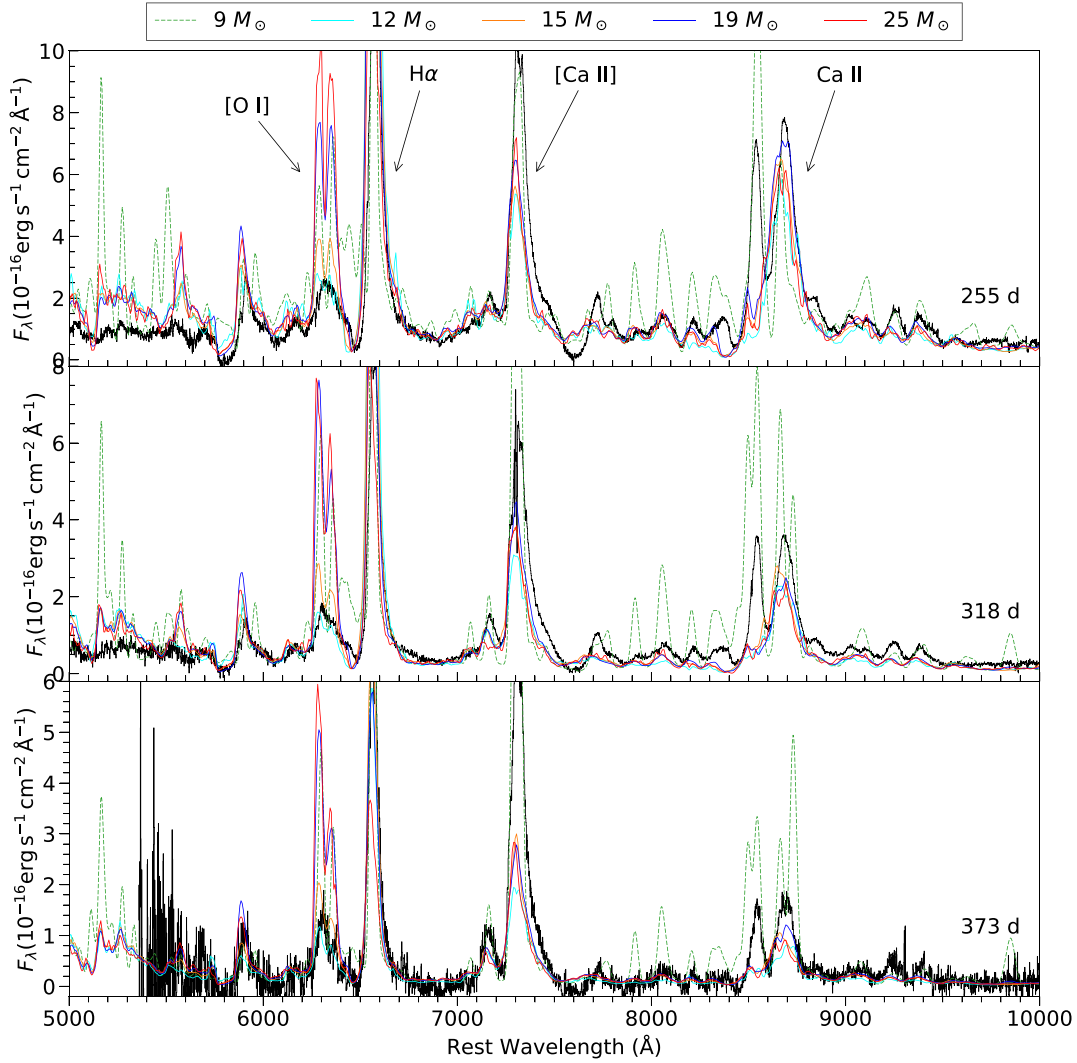


**Figure 11.** Nebular spectra of SN 2020fqv at 255 (top), 318 (middle), and 373 (bottom) days post-explosion. Flux calibration is obtained by comparing the synthetic photometry from these spectra with the interpolated observed  $r$  band photometry. Nebular spectra models from Jerkstrand et al. (2014) for  $M_{\text{ZAMS}} = 12, 15, 19,$  and  $25 M_{\odot}$  and the  $9 M_{\odot}$  models from Jerkstrand et al. (2018) are overplotted for comparison. Significant emission lines ([O I],  $H\alpha$ , [Ca II], and Ca II triplet) are annotated. See Section 3.4.3 for how these models have been scaled to match SN 2020fqv. The 12 and  $15 M_{\odot}$  models provide the best fit to our data.

by computing

$$\int F_{\lambda}(\lambda)T(\lambda)d\lambda / \int T(\lambda)d\lambda, \quad (2)$$

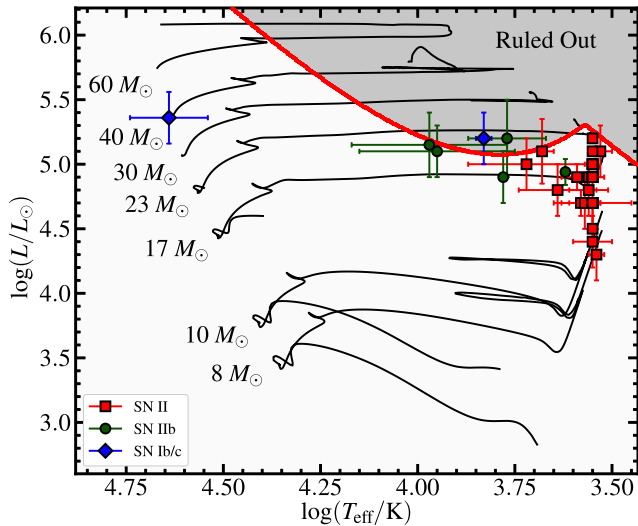
where  $F_{\lambda}$  is the flux spectrum and  $T(\lambda)$  is the filter transmission profile. We then scale to spectrum to match the synthetic photometry with the observed photometry interpolated to the spectrum's epoch. We account for dust extinction in both the photometry and the spectra.

Fig. 11 shows the spectra with models overplotted. The models at four different masses generally predict similar line luminosity for the calcium lines: both the IR triplet and the [Ca II] 7292, 7324 Å. We note that the discrepancy between the model and the IR triplet profile of SN 2012aw has been noted in the original study (Jerkstrand et al. 2014). The main discriminating feature between the four models is the luminosity of the [O I] 6300, 6364 Å lines, since the oxygen mass has been shown to be proportional to the ZAMS mass (e.g. Dessart & Hillier 2011; Jerkstrand et al. 2014). From the three epochs of data, models with  $M_{\text{ZAMS}} = 12$  and  $15 M_{\odot}$  are favoured over the 19 and  $25 M_{\odot}$  models. The low-mass  $9 M_{\odot}$  models predict stronger line

emissions than what is observed. This is likely due to the fact that the models have been scaled up by a large factor to make up for the small  $^{56}\text{Ni}$  mass assumed in the model. The inferred progenitor mass is consistent with the progenitor mass inferred from light-curve fitting. We also note that the models predict the continuum flux level of SN 2020fqv well, especially in the blue, showing that our reddening correction is reasonable. From these independent measurements, we conclude that the progenitor star of SN 2020fqv is an average mass RSG with  $M_{\text{ZAMS}}$  around  $12\text{--}15 M_{\odot}$ .

#### 3.4.4 Progenitor mass limit from pre-explosion imaging non-detection

The flux upper limits of a pre-explosion counterpart to SN 2020fqv from Table 4 allow us to constrain the properties of the progenitor star of this SN. Assuming consistent Milky Way extinction and interstellar host extinction as in Section 3.1, we model hypothetical counterparts to SN 2020fqv as blackbodies with a fixed intrinsic luminosity and temperature. Following methods described in Kil-



**Figure 12.** Hertzsprung–Russell diagram showing the parameter space for which we rule out a pre-explosion counterpart to SN 2020fqv using the limiting magnitudes in Table 4. The grey region is ruled out while stars occupying the remainder of the diagram are allowed. For comparison, we show SN progenitor stars including red supergiant progenitor stars to Type II SNe (Smartt 2015), red and yellow supergiant progenitors to Type IIb SNe (Aldering, Humphreys & Richmond 1994; Crockett et al. 2008; Maund et al. 2011; Van Dyk et al. 2014; Kilpatrick et al. 2017), and the progenitor systems of the Type Ib SNe iPTF13bvn (Cao et al. 2013) and SN 2019yvr (Kilpatrick et al. 2021). We also overplot single-star evolutionary tracks from the MESA Isochrones & Stellar Tracks code (Choi et al. 2016).

patrick et al. (2021), we then forward model this spectral energy distribution assuming a host extinction, redshift, distance, Milky Way extinction, and filter transmission functions consistent with our previous analysis. If any of the derived magnitudes in *HST*/WFPC2 F606W, *Spitzer*/IRAC Channels 1 and 2, or PS1/GPC1 *grizy* are brighter than those given in Table 4, we consider that model ruled out.

The results of this analysis are shown in Fig. 12. We can rule out most evolved and terminal massive stars with  $\log(L/L_{\odot}) > 5.1$ , including the yellow supergiant progenitors to SN 2008ax and SN 2019yvr (Crockett et al. 2008; Kilpatrick et al. 2021). However, most known RSG progenitor stars are allowed by our limits, including all verified RSG detections in Smartt (2009, 2015). Quantitatively, our limits correspond to  $\log(L/L_{\odot}) \approx 5.1$  along the RSG branch where  $T_{\text{eff}} \approx 3450$  K. Thus, following single-star evolutionary tracks from the MESA Isochrones & Stellar Tracks code (MIST; Choi et al. 2016), we find that our limits rule out red supergiant progenitors with  $M_{\text{ZAMS}} > 17 M_{\odot}$ .

### 3.5 Circumstellar medium interaction

#### 3.5.1 Early excess flux from CSM interaction

In this section we attempt to explain the early excess flux observed in SN 2020fqv, assuming that the CSM around the progenitor originated from an outburst caused by wave heating during late-stage nuclear burning (Quataert & Shiode 2012; Fuller 2017; Wu & Fuller 2021). We note that the mechanism of CSM formation has not been established yet, and different scenarios are possible, but this approach proved fruitful in our earlier work on SN 2017eaw (Morozova et al. 2020). In this approach, we first pre-heat an RSG model by launching a weak shock wave through its envelope, which leads to the ejection

of outermost material. As this material expands, we collect the snapshots of its profile, which extends from the stellar surface out to some outer radius. We later model the interaction between the SN shock with this CSM.

Both initial pre-heating of the RSG star and the final SN explosion are modelled with the publicly available code SNEC (Morozova et al. 2015). We work with a solar metallicity,  $15 M_{\odot}$  (at zero-age main sequence, ZAMS) stellar evolution model from the KEPLER set by Sukhbold et al. (2016), evolved to the pre-collapse RSG stage. To pre-heat the star we inject energy  $E_{\text{inj}}$  at the base of its hydrogen envelope with the values between  $1.0 \times 10^{46}$  and  $10.5 \times 10^{46}$  erg, in steps of  $0.5 \times 10^{46}$  erg. These values of  $E_{\text{inj}}$  are chosen based on the models of vigorous late-stage nuclear burning episodes (core Ne or O burning) described for a similar solar-metallicity  $15 M_{\odot}$  MESA model in Fuller (2017). The snapshots of pre-heated density profiles are collected every  $\sim 20$  d while we track the dynamics of the resulting outburst until  $\approx 900$  d after the energy injection. Finally, the obtained grid of models in  $E_{\text{inj}}$  and  $t_{\text{inj}}$  (time since the energy injection) is exploded in a regular core-collapse SN set-up with final energy  $E_{\text{fin}} = 0.5 \times 10^{51}$  erg and radioactive  $^{56}\text{Ni}$  mass  $M_{\text{Ni}} = 0.043 M_{\odot}$  mixed uniformly up to  $7 M_{\odot}$  in mass coordinate.

In addition to bolometric luminosity, SNEC outputs colour light curves computed from a blackbody spectrum taken at the photospheric temperature. At early times (first  $\sim 30$  d of the light curve), when the photospheric temperature exceed  $\sim 8000$  K, the SN spectra are sufficiently close to the black body spectra. However, as the temperature of the ejecta decreases to  $\sim 6500$  K (plateau part), the blue part of the spectrum becomes affected by the blanketing from large number of iron group lines (see Kasen & Woosley 2009). To correct our light curves for this effect we post-process the output of SNEC with the spectral code SYNOW (Thomas, Nugent & Meza 2011).<sup>12</sup> Namely, we construct SYNOW spectra using ejecta velocities and temperatures returned by SNEC, and obtain the colour light curves in different observed bands from these spectra using the filter profiles. The best-fitting model is determined from comparing the obtained colour light curves to the observed magnitudes of SN 2020fqv and looking for the minimum of  $\chi^2$ .

The results of our modelling are shown in Fig. 13. The best-fitting model is shown in the middle panel of Fig. 13, and the top panel shows the colour coded distribution of  $\ln(\chi^2/\chi_{\text{min}}^2)$ . The best agreement with the observations is seen for  $E_{\text{inj}} = 4.5 \times 10^{46}$  and  $t_{\text{inj}} = 300$  days, which would correspond to an eruption about  $\sim 200$  d before the SN.<sup>13</sup> While our search of archival data from ATLAS and ZTF shows no such eruption, it may be fainter than the detection limit due in part to the considerable extinction in the direction of SN 2020fqv. The error bars in the bottom panel are constructed from all light curves that are within the white dashed rectangle shown in the top panel. The dashed lines show the blackbody magnitudes returned by SNEC, while the solid lines are computed from SYNOW spectra. The difference between the two is generally minor, apart from the late *g*-band light curve, where the iron line blanketing effect is expected to be the strongest. Note that we did not perform a broader study across different progenitor masses and final SN energies, which could result in a slightly better fit.

The bottom panel of Fig. 13 justifies the need to pre-heat the RSG models by a weak shock wave before simulating the SN explosion,

<sup>12</sup><https://c3.lbl.gov/es/>

<sup>13</sup>These parameters are very similar to the ones obtained from the same analysis for SN 2017eaw in Morozova et al. (2020). There, the best-fitting energy is  $E_{\text{inj}} = 5 \times 10^{46}$  erg, and the time is  $t_{\text{inj}} = 297$  d.

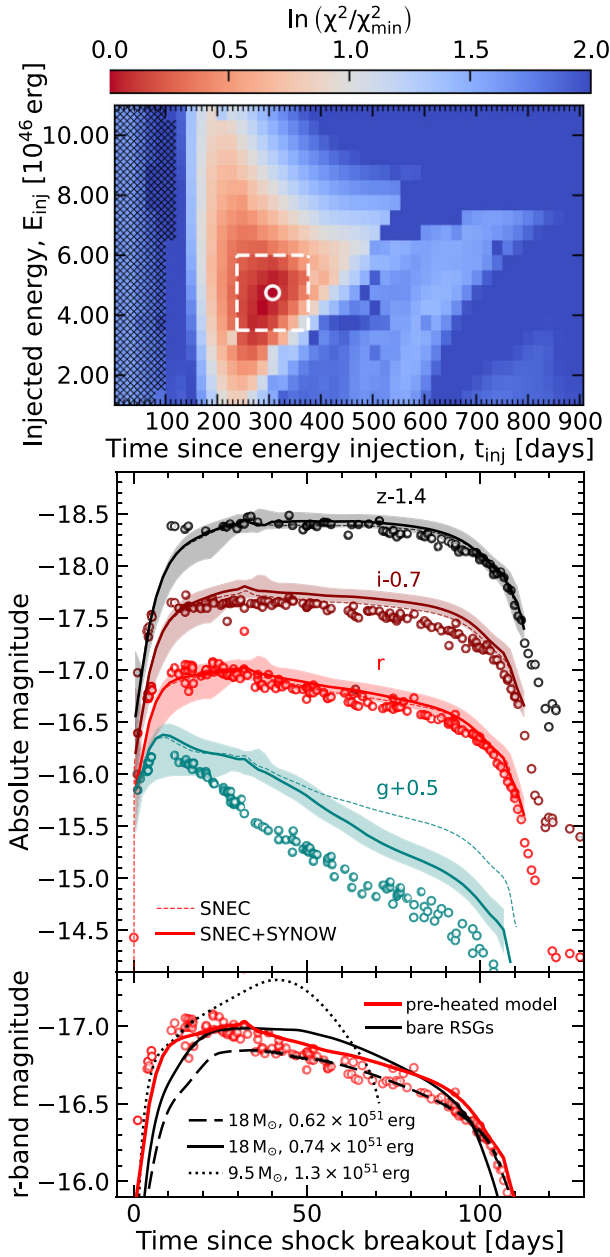


**Figure 13.** *Top panel:* Colour-coded distribution of  $\ln(\chi^2/\chi_{\min}^2)$  across the  $E_{\text{inj}}-t_{\text{inj}}$  parameter space. The black cross-hatched region covers the times during which the weak shock wave launched by the energy injection has not yet reached the stellar surface. All final SN explosions are performed with the same set of parameters,  $E_{\text{fin}} = 0.5 \times 10^{51}$  erg and  $M_{\text{Ni}} = 0.043 M_{\odot}$ . The white circle shows the minimum  $\chi^2$ , while the dashed white rectangle outlines the models that were used to construct the error bars in the bottom panel. *Middle panel:* The colour light curves of the best fitting model, compared to the data of SN 2020fqv. Dashed lines show the magnitudes returned by SNEC, while the solid curves are obtained by post-processing SNEC output with SYNOW. The error bars correspond to the area between all light curves within the white rectangle in top panel. *Bottom panel:* The  $r$ -band light curve of our best fitting model (solid red line) together with the data of SN 2020fqv. For comparison, the black lines show our best attempts to fit the  $r$ -band data with the bare RSG models that were not pre-heated by a weak shock wave before the full SN explosion. The dashed, solid, and dotted black curves aim to fit the data in the time intervals 35–110, 0–110, and 0–20, respectively.

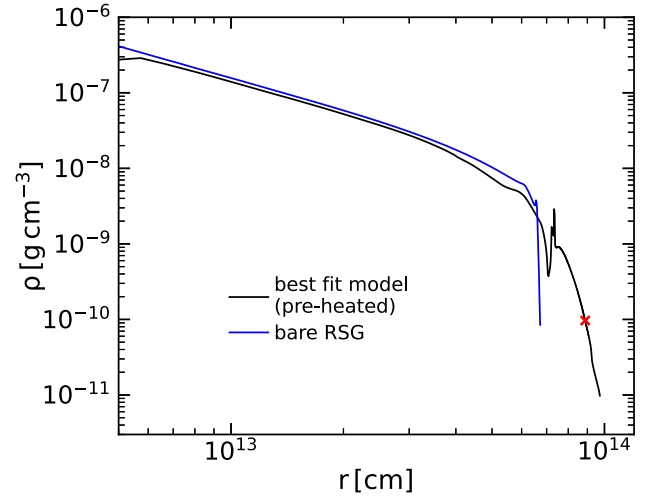


**Figure 14.** The density profile of the progenitor star of SN 2020fqv and its CSM at the time of explosion. This density profile is used in Fig. 13. The red cross marks the location in the CSM where the SN shock finally breaks out and the SN becomes observable.

producing a density profile shown in Fig. 14. In that panel, we plot only  $r$ -band light curves, but the other filters would show a similar picture. The red solid curve shows our best-fitting model from the panel above, while the black curves show the ‘fits’ that we obtained for the same data from the bare RSG models that were not pre-heated and did not form a dense CSM. Specifically, the dashed line shows the model that fits best the  $r$ -band magnitude in days 35–110 after the shock breakout, the dotted line fits the data in days 0–20 after the shock breakout, and the solid black line aims to fit the entire data between day 0 and day 110 of the light curve.<sup>14</sup> The figure shows that none of the bare RSG models can fit the fast early rise of SN 2020fqv light curve and its plateau part at the same time. Pre-heating the model, even though it does not provide the perfect fit to the data, changes the shape of the simulated light curve that brings it in a better agreement with the data.

In Fig. 15, we compare our models to the *TESS* data for SN 2020fqv. The best-fitting model from Fig. 13 is represented there by solid lines. In that model, injection of  $E_{\text{inj}} = 4.5 \times 10^{46}$  at the base of the hydrogen envelope led to the ejection of the outer layers of the star and formation of the CSM. For comparison, the dashed line represents the light curve of the bare RSG model that can fit the  $r$ -band magnitude of SN 2020fqv during days 35–110 of the light curve. The plots show that pre-heating the model noticeably improves its agreement with the data in the early part of the light curve. At the same time, even the pre-heated model does not rise sufficiently fast when compared to the *TESS* light curve, which suggests that further modifications to the theoretical models should be considered.

On the other hand, it is possible to find a bare RSG model that fits the early *TESS* data without a CSM. The dotted line in Fig. 15 represents the model that fits best the first 20 d of the  $r$ -band light curve, providing a good fit to the *TESS* data as well (this model is the same as the one shown by the dotted black line in the bottom panel of Fig. 13). This model has ZAMS mass of  $9.5 M_{\odot}$  and final energy of

<sup>14</sup>All three black light curves show the blackbody magnitudes returned by SNEC. However, as can be seen from the middle panel of Fig. 13, post-processing SNEC output with SYNOW changes the  $r$ -band light curve only slightly.

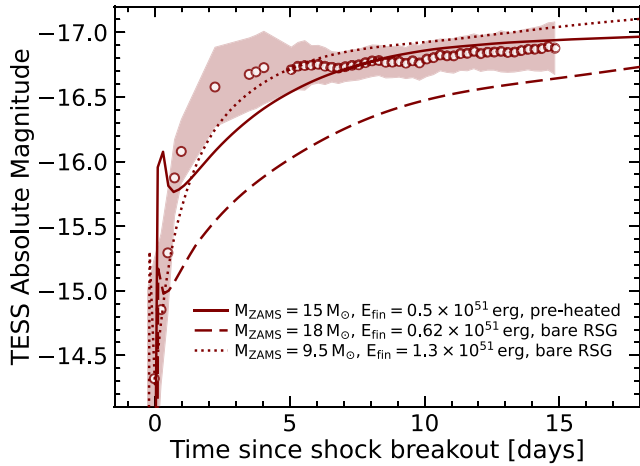


**Figure 15.** *TESS* light curve of SN 2020fqv compared to the numerical models. The solid line represents the best-fit model from Fig. 13, in which the energy injection led to the formation of a CSM. The early spike seen in the model is a numerical artefact due to the fact that the photosphere is not resolved in our simulations during the first several hours of the light curve. Both dashed and dash-dotted lines represent the light curves of bare RSG models. The dashed line represents the model that provides the best fit for the *r*-band magnitude during days 35–110 of the light curve, while the dash-dotted line fits best the first 15 d of the light curve. The corresponding light curves and data in *r*-band are shown in the inset. Even though the dash-dotted line fits well the early *TESS* data, it cannot be regarded as a fit for the entire SN light curve.

$1.3 \times 10^{51}$  erg. However, as shown in Fig. 13, this model continues rising above the data and demonstrates too short of a plateau to be regarded as a fitting model for SN 2020fqv. Indeed, for example, in Pumo et al. (2017) and Morozova et al. (2018) it was shown that the final energies needed to reproduce plateau lengths of typical SNe II-P lay below  $\sim 1.0 \times 10^{51}$  erg. For this reason, we conclude that it is challenging to infer the SN parameters based on the early data only, and it is important to take into account the entire light curve.

From the best-fitting models to the early-time light curve, we can infer the density profile of the progenitor star and the CSM, which is shown in Fig. 14. The CSM is so optically thick that the shock breakout does not happen at the edge of the stellar envelope, but inside the CSM. The red cross in Fig. 14 marks the location of the shock break-out, at about  $9 \times 10^{13}$  cm, about  $2.5 \times 10^{13}$  cm ( $360 R_{\odot}$ ) above the stellar envelope. With the CSM, the shock breakout happens at a lower density than it would in a bare RSG envelope due to the more gradual density gradient in the CSM. Thus, the shocked material is able to expand and cool faster, resulting in an early time excess flux compared to what is expected in a SN from a bare RSG progenitor. This material is responsible for filling the ‘gap’ seen in the bottom panel of Fig. 13 between the dashed bare RSG model and the data in the first 30 d since shock breakout.

Finally, it is informative to compare the characteristics of the model that fits SN 2020fqv to a larger set of models studied in Morozova et al. (2018). In that work, the authors found numerical fits to the light curves of 20 well-studied SNe II-P by adding the CSM to their RSG models artificially in the form of a dense wind. The CSM masses that were needed in order to fit the early data varied between 0.003 and  $0.83 M_{\odot}$ , while the external radii of the CSM varied between 700 and  $2200 R_{\odot}$  for different SNe.

We start from estimating the external radius of the CSM in our best-fitting model for SN 2020fqv. The radius of the original RSG

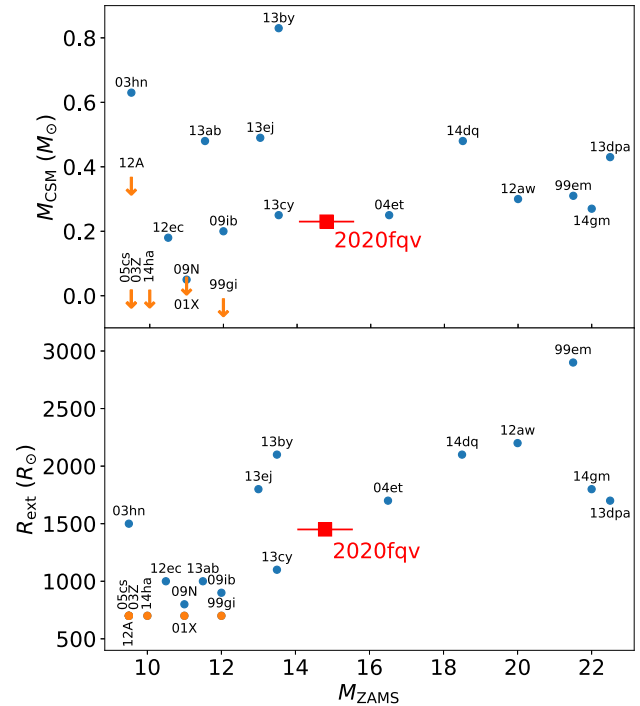


**Figure 16.** Inferred CSM mass (top) and outer radius (bottom) as a function of  $M_{ZAMS}$  of SN 2020fqv compared with other SNe II-P from Morozova et al. (2018). The error bar in  $M_{ZAMS}$  of SN 2020fqv is from comparing different mass measurements in this work. Orange markers denote events with no detected CSM;  $R_{ext}$  measures the size of the progenitor for those events.

model is  $841 R_{\odot}$  (which is also the inner radius of the CSM), while the radius of our best-fitting model prior to the SN explosion is  $1450 R_{\odot}$ . This external radius is in agreement with the CSM radii estimated in Morozova et al. (2018). Since the best-fitting model for SN 2020fqv corresponds to  $t_{inj} \approx 300$  d ( $\approx 200$  d between the pre-explosion outburst and the SN), we estimate the velocity of CSM to be  $v_{CSM} \approx 24$  km  $s^{-1}$ . The best-fitting model for SN 2020fqv corresponds to pre-heating energy  $E_{inj} = 4.5 \times 10^{46}$  erg, but only a fraction of this energy goes into the kinetic energy of the outflow ( $E_{kin} \approx 1.4 \times 10^{45}$  erg in our simulation). Estimating the CSM mass from the formula  $2E_{kin}/v_{CSM}^2$  we obtain  $M_{CSM} \approx 0.23 M_{\odot}$ . This CSM mass lays within the range of values obtained in Morozova et al. (2018), and it is very close to the CSM mass obtained there for SN 2004et ( $0.25 M_{\odot}$ ). Fig. 16 compares the CSM properties of SN 2020fqv to those of SNe II-P in Morozova et al. (2018); showing that the CSM around SN 2020fqv is ordinary among the population of SNe II-P.

### 3.5.2 Early-time spectroscopy

Fig. 17 shows early time spectra from 1.1 to 3.52 d of SN 2020fqv. For these spectra, a reddened blackbody continuum is fit and subtracted to highlight the emission lines. We tentatively identify narrow H  $\alpha$  emission; however, it is likely due to the host galaxy as it persisted throughout the plateau phase. No other Balmer lines are present. The prominent emission feature that is likely from the SN is the emission around  $4600 \text{ \AA}$ . This feature appears in all the early-time spectra. Fig. 3 clearly shows that it weakens quickly and completely disappears by 11 d. This emission feature is likely a blend between C III, N III, and He II. The strength of these high-

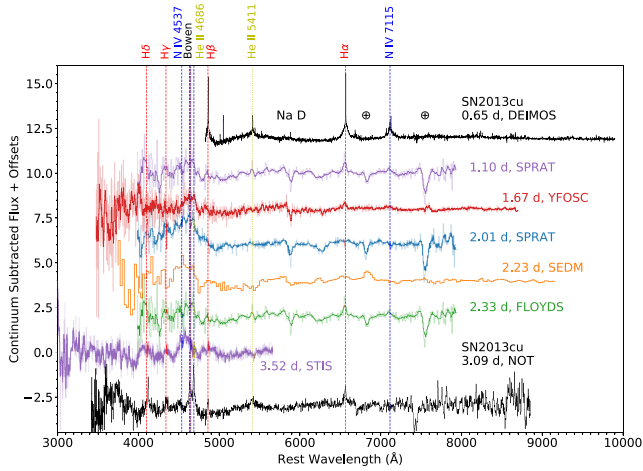


**Figure 17.** Early spectra of SN2020fqv from 1.1 to 3.52 d post-explosion, compared with the prototypical flash-ionization event SN2013cu (Gal-Yam et al. 2014). Solid lines are smoothed spectra; transparent lines are unsmoothed. All spectra have been continuum subtracted to highlight emission lines. Line identifications are provided. The emission feature around 4600 Å marked ‘Bowen’ are the blend of C III 4647, 4650 Å, and N III 4634, 4641 Å, excited likely via the Bowen fluorescence mechanism.

ionization lines relative to the Balmer series indicated that they are not excited thermally, but perhaps by the Bowen fluorescence mechanism (Bowen 1935). In this process, the C III and N III ions are excited by the He II 304 Å emission, and cool via the C III 4647, 4650 Å and N III 4634, 4641 Å lines. However, we note that the STIS spectrum may require N IV 4537 Å emission to explain the emission feature. Fig. 17 also shows spectra at 0.65 and 3.09 d post-explosion of SN2013cu, the prototypical SN with narrow lines in early spectra, the so-called flash ionization features (Gal-Yam et al. 2014). By comparison, it is clear that the narrow lines in SN2020fqv are much weaker than those in SN2013cu with no clear electron-scattering wings, pointing to weaker interactions. Because of the large optical depth of the CSM around SN2020fqv, these narrow lines must emerge from the outer part of the CSM, above the location of shock breakout shown in Fig. 14 ( $> 9 \times 10^{13}$  cm).

### 3.5.3 High-velocity component in the $H\alpha$ line

Fig. 18 shows the evolution of the  $H\alpha$  line profile from 50 to 111 d in the latter half of the plateau phase. The P-Cygni absorption trough slowed down from 6500 to 5000  $\text{km s}^{-1}$  as the photosphere receded into the slower ejecta. We identified a persistent high-velocity (HV) absorption feature at about  $-12\,900 \text{ km s}^{-1}$ . This velocity corresponded to the wavelength of 6280 Å, at which there was no other lines. Such an absorption component could arise from an ongoing CSM interaction, as the high-energy photons from the interaction continuously excited the outer, fast-moving ejecta (Chugai et al. 2007). Because this feature persisted until the end of the plateau phase, it was not likely due to time-dependent effects (Dessart & Hillier 2008). Since this feature is persistent, it could not have come from the same inner CSM component responsible for the early flux excess and the early-time narrow emission lines. It is a more extended CSM likely formed by the RSG wind.

HV absorption components of strong spectral lines have been observed in a number of SNe II-P. Gutiérrez et al. (2017) found that the absorption at around this wavelength is due to the Si II 6355 Å line in the early plateau phase ( $\lesssim 35$  d), and due to the HV component

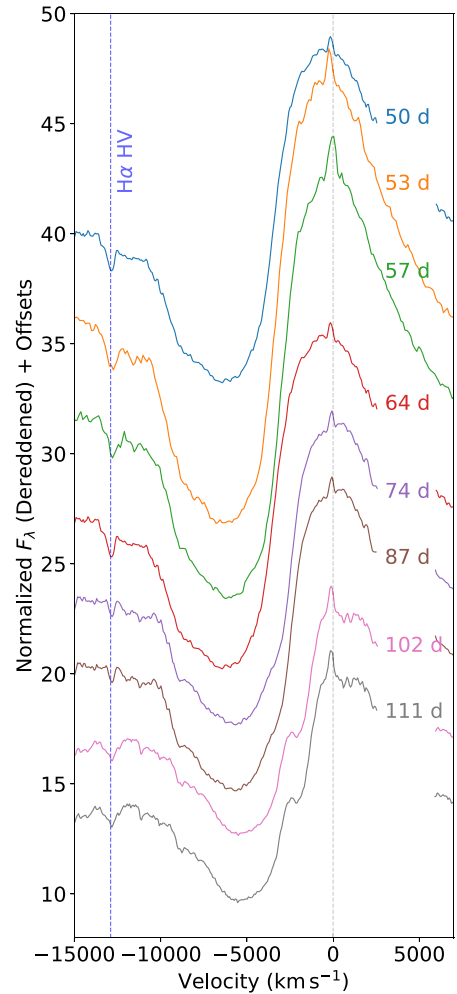


**Figure 18.** The profile of the  $H\alpha$  line in the latter half of the plateau phase, plotted in velocity space. The zero velocity is marked with a dashed grey line; the narrow component at this position is from the host galaxy. We identify a persistent absorption at a constant velocity of  $-12\,900 \text{ km s}^{-1}$  (marked with a dashed blue line), likely due to the outer ejecta being excited by ongoing CSM interactions. This is in contrast with the velocity of the absorption trough of the P-Cygni profile, whose speed decreases towards the end of the plateau phase.

of  $H\alpha$  later in the plateau phase. However, the better place to clearly detect the HV component is the He I 1.083  $\mu\text{m}$  because there is less contamination from other lines at those wavelengths for SNe II-P. The HV component of the He I 1.083  $\mu\text{m}$  line has been detected in virtually all SNe II-P with near-IR spectroscopy (e.g. Tinyanont et al. 2019a; Davis et al. 2019), indicating that CSM interactions at this level is common. In fact, Davis et al. (2019) listed the presence of the HV component of the He I 1.083  $\mu\text{m}$  line as a feature distinguishing SNe II-P from II-L.

### 3.6 Comparison with other SNe II with early UV spectra

UV spectroscopic observations of SNe II remain sparse as only *HST* STIS and COS have adequate sensitivities. The UV flux also fades quickly in SNe II-P due to Fe line blanketing. Fig. 19 shows UV-to-optical spectra of SN2020fqv from 11 and 17 d post-explosion, in comparison to two other SNe II-P. SN1999em was observed with *HST*/STIS at 12 d post-explosion (Baron et al. 2000),

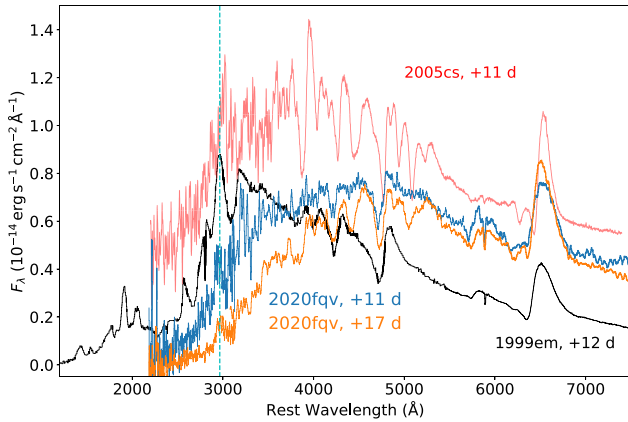


**Figure 19.** UV to optical spectra of SN 2020fqv from 11 and 17 d post-explosion. Similar spectra of SNe 1999em (Baron et al. 2000) and 2005cs (Bufano et al. 2009) are plotted for comparison. The 2965 Å feature due to Fe-line blanketing is marked by a dashed cyan line; the feature is visible in all spectra. These are the only SNe II-P with high-quality early-time UV spectra available in the literature. All spectra have been corrected for reddening. The flux scale is based on the calibrated *HST* spectra of SN 2020fqv. The literature spectra are scaled for visualization.

while SN 2005cs was observed with *Swift* UV grism at 11 d post-explosion (Bufano et al. 2009). These are the only UV spectra of SNe II-P available in the literature at comparable epochs with comparable wavelength coverage. We note that SN 2005ay also has UV spectroscopy at around 12 d post-explosion obtained by the *Galaxy Evolution Explorer (GALEX)* (Gal-Yam et al. 2008), but the spectra only cover up to 2900 Å. Lastly, Dhungana et al. (2016) presented several epochs of UV spectroscopy of SN 2013ej, showing similar spectral shape and features as other SNe II-P observed at similar epochs.

The only discernible spectral feature of SN 2020fqv in the UV is the feature at 2965 Å, most visible in the +17 d spectrum. This peak is due to Fe line blanketing, absorbing the continuum flux on either side of it. The presence of this feature demonstrates that line blanketing starts to play a role already at +11 d for SN 2020fqv. This feature is also present in the spectrum of SN 1999em; however, the UV flux in SN 1999em is not yet as strongly absorbed as is the case in SN 2020fqv. This may be because SN 1999em synthesized less  $^{56}\text{Ni}$  ( $\sim 0.02 M_{\odot}$ ; Elmhamdi et al. 2003) compared to that of SN 2020fqv ( $0.043 M_{\odot}$ ). SN 2005cs shows a similarly strong Fe line blanketing in the UV, even though it only synthesized  $0.003\text{--}0.008 M_{\odot}$  of  $^{56}\text{Ni}$  (Utrobin & Chugai 2008; Pastorello et al. 2009). It is, however, a sub-luminous SN II-P resulting from a low mass ( $\sim 9 M_{\odot}$ ) progenitor star (Maund, Smartt & Danziger 2005; Li et al. 2006; Smartt 2009). With the low ejecta mass, the spectral features emerge much earlier compared to SN 2020fqv, including the Fe-line blanketing. While early UV spectroscopy can directly measure the abundance of Fe-peak elements and the opacity evolution of the ejecta (e.g. Foley & Kirshner 2013), observations are presently sparse and a meaningful comparison cannot be made. Future *HST/STIS* observations within  $\sim$ week of the explosion are needed to fully probe the landscape of early UV emissions in CCSNe.

#### 4 CONCLUSIONS

Despite being the most common subtype of CCSNe, type II-P SNe still harbour many mysteries as recent observations uncover phenomena unexplained by simple models of RSG explosions in

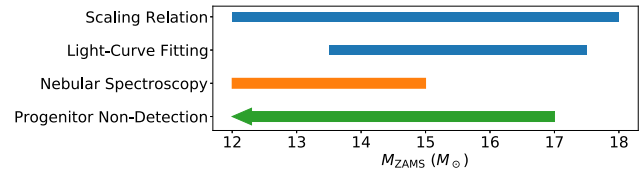


**Figure 20.** A summary of different progenitor mass estimates presented in this work. Different colours represent the different types of methods used to constrain the progenitor mass: blue is light-curve fitting, orange is nebular spectroscopy, and green is pre-explosion imaging. All measurements agree that SN 2020fqv is an explosion of an average-mass RSG with  $M_{\text{ZAMS}}$  around  $13.5\text{--}15 M_{\odot}$ .

a vacuum. In this work, we present the explosion parameters of the nearby SN 2020fqv. With the high-cadence *TESS* data, we are able to determine the explosion epoch to within 4 h and monitor its early photometric evolution. From the bolometric light curves, we measure the mid-plateau (50 d post-explosion) luminosity of  $L_{50} = (1.3 \pm 0.3) \times 10^{42} \text{ erg s}^{-1}$  and the plateau length of  $t_p = 114 \pm 1 \text{ d}$ . We determine the kinetic energy of the explosion to be  $(4.1 \pm 0.1) \times 10^{50} \text{ erg}$  and the  $^{56}\text{Ni}$  mass is  $0.043 \pm 0.017 M_{\odot}$ . The progenitor mass is obtained by four different methods: simple scaling relation; light-curve fitting; nebular spectroscopy; and pre-explosion imaging non-detection. Fig. 20 compares the ranges of progenitor mass estimates obtained from the four methods, pointing to a  $\sim 13.5\text{--}15 M_{\odot}$  RSG as the progenitor of SN 2020fqv. This is a typical mass for a RSG progenitor to SNe II-P (e.g. Smartt et al. 2009).

We then show that SN 2020fqv exhibits many signatures of shock interactions with a CSM ejected prior to the explosion. SN 2020fqv rises to its peak luminosity too quickly to be explained by a typical RSG explosion model without CSM. Light curve fitting shows that the rise can be explained by an interaction between the SN shock and the CSM ejected in a pre-SN eruption with  $4.5 \times 10^{46} \text{ erg}$  injected into the base of the hydrogen envelope about 300 d pre-explosion. The (unobserved) eruption ejects  $\sim 0.23 M_{\odot}$  of materials in to the CSM with the maximum radius of  $\sim 1450 R_{\odot}$ . Fig. 16 shows that these CSM properties are typical among SNe II-P. Early spectra show narrow emission lines from high-ionization metal species (C III, N III, N IV) and He II around 4600 Å from this CSM. Some of these lines may be excited by the Bowen fluorescence mechanism (Bowen 1935). Throughout the plateau phase, the H  $\alpha$  line shows a persistent high-velocity component at a constant velocity of  $-12\,900 \text{ km s}^{-1}$ , likely due to the continuous CSM interaction exciting the outermost (and fastest moving) layer of the ejecta.

These observations add to the mounting evidence that RSGs can explode with a substantial amount of CSM, more than what is expected from a standard RSG wind ( $\sim 10^{-6} M_{\odot} \text{ yr}^{-1}$  versus  $0.23 M_{\odot}$  in less than a year observed here). This indicates that the late-stage evolution of massive stars is more complicated than what is previously thought. Even for RSGs whose evolution is not significantly affected by binary interactions (though see Zapartas et al. 2019, 2021), mass-loss due to the late-stage nuclear fusion can still produce a CSM with diverse properties that interacts with the SN shock at early times (Quataert & Shiode 2012; Fuller 2017; Wu & Fuller 2021). While studies of CSM properties with moderately-sized samples of SNe II-P are present (e.g. Morozova et al. 2018), the Vera Rubin Observatory will be able to produce multiband light curves of all SNe II-P out to about 400 Mpc, allowing for a truly systematic study of CSM interactions around SNe II-P. With the pre-detection of SNe II-P progenitors reliant on serendipitous pre-explosion *HST* imaging, if a connection between the CSM properties and progenitor

properties can be made, this would greatly enhance our capability to study the late-stage evolution of RSGs.

## ACKNOWLEDGEMENTS

We thank Thomas de Jaeger for a discussion on the colour of type II SNe and for providing us some data.

The script to colourize the single-band pre-explosion *HST* image is based on a script written by M. Durbin, which can be found here: <https://gist.github.com/meredith-durbin/c05bba9490017ad8e5bb7fd2d9774d04>. This work has made use of the SVO Filter Profile Service (<http://svo2.cab.inta-csic.es/theory/fps/>) supported from the Spanish MINECO through grant AYA2017-84089.

The UCSC team is supported in part by NASA grant 80NSSC20K0953, NSF grant AST-1815935, the Gordon & Betty Moore Foundation, the Heising-Simons Foundation, and by a fellowship from the David and Lucile Packard Foundation to RJF. MRS is supported by the NSF Graduate Research Fellowship Program Under grant 1842400. DAC acknowledges support from the National Science Foundation Graduate Research Fellowship under grant DGE1339067. Support for this work was provided by NASA through the NASA Hubble Fellowship grant HF2-51462.001 awarded by the Space Telescope Science Institute, which is operated by the Association of Universities for Research in Astronomy, Inc., for NASA, under contract NAS5-26555.

This work is based on observations made with the NASA/ESA *Hubble Space Telescope* under programme number GO-15876 and data from programme number GO-5446 obtained from the data archive at the Space Telescope Science Institute. Support for programme GO-15876 was provided by NASA through a grant from STScI, which is operated by AURA, Inc., under NASA contract NAS 5-26555. Additional support was provided through NASA grants in support of *Hubble Space Telescope* programmes GO-15889 and GO-16075.

AG is supported by the National Science Foundation Graduate Research Fellowship Program under grant no. DGE-1746047. AG also acknowledges funding from the Center for Astrophysical Surveys Fellowship at UIUC/NCSA and the Illinois Distinguished Fellowship. CDK acknowledges support through NASA grants in support of *Hubble Space Telescope* programme AR-16136. WJ-G is supported by the National Science Foundation Graduate Research Fellowship Program under Grant No. DGE-1842165 and the IDEAS Fellowship Program at Northwestern University. IP-F acknowledges support from the Spanish State Research Agency (AEI) under grant numbers ESP2017-86852-C4-2-R and PID2019-105552RB-C43. FP acknowledges support from the Spanish State Research Agency (AEI) under grant number PID2019-105552RB-C43. QW acknowledges financial support provided by the STScI Director's Discretionary Fund.

This paper includes data collected by the TESS mission. Funding for the TESS mission is provided by the NASA's Science Mission Directorate.

Some of the data presented herein were obtained at the W. M. Keck Observatory, which is operated as a scientific partnership among the California Institute of Technology, the University of California, and NASA. The Observatory was made possible by the generous financial support of the W. M. Keck Foundation.

This work is based in part on observations obtained at the international Gemini Observatory, a program of NSF's NOIRLab (programmes GN-2020A-Q-134 and GS-2020A-Q-128), which is managed by the Association of Universities for Research in Astronomy (AURA) under a cooperative agreement with the National Sci-

ence Foundation. on behalf of the Gemini Observatory partnership: the National Science Foundation (United States), National Research Council (Canada), Agencia Nacional de Investigación y Desarrollo (Chile), Ministerio de Ciencia, Tecnología e Innovación (Argentina), Ministério da Ciência, Tecnologia, Inovações e Comunicações (Brazil), and Korea Astronomy and Space Science Institute (Republic of Korea).

This work was enabled by observations made from the Gemini North and Keck telescopes, located within the Maunakea Science Reserve and adjacent to the summit of Maunakea. The authors wish to recognize and acknowledge the very significant cultural role and reverence that the summit of Maunakea has always had within the indigenous Hawaiian community. We are grateful for the privilege of observing the Universe from a place that is unique in both its astronomical quality and its cultural significance.

A major upgrade of the Kast spectrograph on the Shane 3 m telescope at Lick Observatory was made possible through generous gifts from the Heising-Simons Foundation as well as William and Marina Kast. Research at Lick Observatory is partially supported by a generous gift from Google.

This work makes use of observations from the Las Cumbres Observatory global telescope network following the approved NOIRLab programmes 2020A-0196, 2020A-0334, 2020B-0250, 2020B-0256, 2021A-0135, and 2021A-0239. LCO telescope time was granted by NOIRLab through the Mid-Scale Innovations Program (MSIP). MSIP is funded by NSF.

The Liverpool Telescope is operated on the island of La Palma by Liverpool John Moores University in the Spanish Observatorio del Roque de los Muchachos of the Instituto de Astrofísica de Canarias with financial support from the UK Science and Technology Facilities Council.

This work is based in part on observations obtained with the Samuel Oschin 48-inch Telescope at the Palomar Observatory as part of the Zwicky Transient Facility project. ZTF is supported by the NSF under grant AST-1440341 and a collaboration including Caltech, IPAC, the Weizmann Institute for Science, the Oskar Klein Center at Stockholm University, the University of Maryland, the University of Washington, Deutsches Elektronen-Synchrotron and Humboldt University, Los Alamos National Laboratories, the TANGO Consortium of Taiwan, the University of Wisconsin at Milwaukee, and the Lawrence Berkeley National Laboratory. Operations are conducted by the Caltech Optical Observatories (COO), the Infrared Processing and Analysis Center (IPAC), and the University of Washington (UW).

This work has made use of data from the Asteroid Terrestrial-impact Last Alert System (ATLAS) project. The Asteroid Terrestrial-impact Last Alert System (ATLAS) project is primarily funded to search for near earth asteroids through NASA grants NN12AR55G, 80NSSC18K0284, and 80NSSC18K1575; byproducts of the NEO search include images and catalogs from the survey area. This work was partially funded by Kepler/K2 grant J1944/80NSSC19K0112 and *HST* GO-15889, and STFC grants ST/T000198/1 and ST/S006109/1. The ATLAS science products have been made possible through the contributions of the University of Hawaii Institute for Astronomy, the Queen's University Belfast, the Space Telescope Science Institute, the South African Astronomical Observatory, and The Millennium Institute of Astrophysics (MAS), Chile.

The Pan-STARRS1 Surveys (PS1) and the PS1 public science archive have been made possible through contributions by the Institute for Astronomy, the University of Hawaii, the Pan-STARRS Project Office, the Max-Planck Society and its participating institutes, the Max Planck Institute for Astronomy, Heidelberg and the

Max Planck Institute for Extraterrestrial Physics, Garching, The Johns Hopkins University, Durham University, the University of Edinburgh, the Queen's University Belfast, the Harvard-Smithsonian Center for Astrophysics, the Las Cumbres Observatory Global Telescope Network Incorporated, the National Central University of Taiwan, STScI, NASA under grant NNX08AR22G issued through the Planetary Science Division of the NASA Science Mission Directorate, NSF grant AST-1238877, the University of Maryland, Eotvos Lorand University (ELTE), the Los Alamos National Laboratory, and the Gordon and Betty Moore Foundation. Pan-STARRS is a project of the Institute for Astronomy of the University of Hawaii, and is supported by the NASA SSO Near Earth Observation Program under grants 80NSSC18K0971, NNX14AM74G, NNX12AR65G, NNX13AQ47G, NNX08AR22G, 20-YORPD 20\_2-0014 and by the State of Hawaii.

Palomar Gattini-IR (PGIR) is generously funded by Caltech, Australian National University, the Mt Cuba Foundation, the Heising Simons Foundation, and the Binational Science Foundation. PGIR is a collaborative project among Caltech, Australian National University, University of New South Wales, Columbia University, and the Weizmann Institute of Science. MMK acknowledges generous support from the David and Lucille Packard Foundation. MMK and Eran Ofek acknowledge the US-Israel Bi-national Science Foundation Grant 2016227. MMK and Jenő L. Sokolowski acknowledge the Heising-Simons foundation for support via a Scialog fellowship of the Research Corporation. MMK and AMM acknowledge the Mt Cuba foundation.

## DATA AVAILABILITY

All spectra presented in this work are available via WISEReP. Other data and data analysis scripts can be obtained from the corresponding author upon a reasonable request.

## REFERENCES

- Adams S. M., Kochanek C. S., Gerke J. R., Stanek K. Z., Dai X., 2017, *MNRAS*, 468, 4968
- Aldering G., Humphreys R. M., Richmond M., 1994, *AJ*, 107, 662
- Ambikasaran S., Foreman-Mackey D., Greengard L., Hogg D. W., O'Neil M., 2015, *IEEE Trans. Pattern Anal. Mach. Intel.*, 38, 252
- Andrews J. E. et al., 2019, *ApJ*, 885, 43
- Arnett W. D., Bahcall J. N., Kirshner R. P., Woosley S. E., 1989, *ARA&A*, 27, 629
- Auchettl K., Lopez L. A., Badenes C., Ramirez-Ruiz E., Beacom J. F., Holland-Ashford T., 2019, *ApJ*, 871, 64
- Baron E. et al., 2000, *ApJ*, 545, 444
- Bellm E. C. et al., 2019, *PASP*, 131, 018002
- Björklund R., Sundqvist J. O., Puls J., Najarro F., 2021, *A&A*, 648, A36
- Boone K., 2019, *AJ*, 158, 257
- Bostroem K. A. et al., 2019, *MNRAS*, 485, 5120
- Bouma L. G., Hartman J. D., Bhatti W., Winn J. N., Bakos G. Á., 2019, *ApJS*, 245, 13
- Bowen I. S., 1935, *ApJ*, 81, 1
- Bradley L. et al., 2020, *astropy/photutils*: 1.0.0. doi:10.5281/zenodo.4044744, <https://doi.org/10.5281/zenodo.4044744>
- Brown T. M. et al., 2013a, *PASP*, 125, 1031
- Brown T. M. et al., 2013b, *PASP*, 125, 1031
- Bufano F. et al., 2009, *ApJ*, 700, 1456
- Cao Y. et al., 2013, *ApJ*, 775, L7
- Chandra P., Chevalier R. A., Chugai N., Milisavljevic D., Fransson C., 2020, *ApJ*, 902, 55
- Choi J., Dotter A., Conroy C., Cantiello M., Paxton B., Johnson B. D., 2016, *ApJ*, 823, 102
- Chugai N. N., Chevalier R. A., 2006, *ApJ*, 641, 1051
- Chugai N. N., Chevalier R. A., Utrobin V. P., 2007, *ApJ*, 662, 1136
- Clocchiatti A. et al., 2001, *ApJ*, 553, 886
- Crockett R. M. et al., 2008, *MNRAS*, 391, L5
- Dastidar R. et al., 2019, *MNRAS*, 490, 1605
- Davies B., Beasor E. R., 2018, *MNRAS*, 474, 2116
- Davies B., Beasor E. R., 2020, *MNRAS*, 493, 468
- Davis S. et al., 2019, *ApJ*, 887, 4
- de Jaeger T. et al., 2018, *MNRAS*, 476, 4592
- De K. et al., 2020, *PASP*, 132, 025001
- Dessart L., Hillier D. J., 2008, *MNRAS*, 383, 57
- Dessart L., Hillier D. J., 2011, *MNRAS*, 410, 1739
- Dhungana G. et al., 2016, *ApJ*, 822, 6
- Dimitriadis G. et al., 2020, *Trans. Ser. AstroNote*, 74, 1
- Dolphin A., 2016, *DOLPHOT: Stellar Photometry*. preprint (ascl:1608.013)
- Dong Y. et al., 2021, *ApJ*, 906, 56
- Elmhadi A. et al., 2003, *MNRAS*, 338, 939
- Filippenko A. V., 1997, *ARA&A*, 35, 309
- Fitzpatrick E. L., 1999, *PASP*, 111, 63
- Flewelling H. A. et al., 2020, *ApJS*, 251, 7
- Foley R. J., Berger E., Fox O., Levesque E. M., Challis P. J., Ivans I. I., Rhoads J. E., Soderberg A. M., 2011, *ApJ*, 732, 32
- Foley R. J., Kirshner R. P., 2013, *ApJ*, 769, L1
- Foley R. J., Smith N., Ganeshalingam M., Li W., Chornock R., Filippenko A. V., 2007, *ApJ*, 657, L105
- Foreman-Mackey D., Hogg D. W., Lang D., Goodman J., 2013a, *PASP*, 125, 306
- Foreman-Mackey D., Hogg D. W., Lang D., Goodman J., 2013b, *PASP*, 125, 306
- Forster F. et al., 2020, *Trans. Name Server Discovery Rep.*, 2020-914, 1
- Fox O. D. et al., 2011, *ApJ*, 741, 7
- Fuller J., 2017, *MNRAS*, 470, 1642
- Gal-Yam A. et al., 2008, *ApJ*, 685, L117
- Gal-Yam A. et al., 2014, *Nature*, 509, 471
- Gal-Yam A., Yaron O., Pastorello A., Taubenberger S., Fraser M., Perley D., 2021, *Trans. Name Ser. AstroNote*, 76, 1
- Garnavich P. M., Tucker B. E., Rest A., Shaya E. J., Olling R. P., Kasen D., Villar A., 2016, *ApJ*, 820, 23
- Gutiérrez C. P. et al., 2017, *ApJ*, 850, 89
- Hinton S. R., 2016, *J. Open Source Softw.*, 1, 00045
- Hiramatsu D. et al., 2021, *ApJ*, 913, 55
- Hook I. M., Jørgensen I., Allington-Smith J. R., Davies R. L., Metcalfe N., Murowinski R. G., Crampton D., 2004, *PASP*, 116, 425
- Jacobson-Galán W. V. et al., 2020, *ApJ*, 898, 166
- Jacobson-Galán Wynn et al. 2021, preprint (arXiv:2109.12136)
- Jencson J. E. et al., 2019, *ApJ*, 886, 40
- Jennings Z. G., Williams B. F., Murphy J. W., Dalcanton J. J., Gilbert K. M., Dolphin A. E., Weisz D. R., Fouesneau M., 2014, *ApJ*, 795, 170
- Jerkstrand A., Ertl T., Janka H. T., Müller E., Sukhbold T., Woosley S. E., 2018, *MNRAS*, 475, 277
- Jerkstrand A., Smartt S. J., Fraser M., Fransson C., Sollerman J., Taddia F., Kotak R., 2014, *MNRAS*, 439, 3694
- Jones D. O. et al., 2021, *ApJ*, 908, 143
- Kasen D., Woosley S. E., 2009, *ApJ*, 703, 2205
- Kee N. D., Sundqvist J. O., Decin L., de Koter A., Sana H., 2021, *A&A*, 646, A180
- Kilpatrick C. D. et al., 2017, *MNRAS*, 465, 4650
- Kilpatrick C. D. et al., 2018, *MNRAS*, 473, 4805
- Kilpatrick C. D. et al., 2021, *MNRAS*, 504, 2073
- Kilpatrick C. D., Foley R. J., 2018, *MNRAS*, 481, 2536
- Laplace E., Göteborg Y., de Mink S. E., Justham S., Farmer R., 2020, *A&A*, 637, A6
- Leung S.-C., Fuller J., 2020, *ApJ*, 900, 99
- Li W., Van Dyk S. D., Filippenko A. V., Cuillandre J.-C., Jha S., Bloom J. S., Riess A. G., Livio M., 2006, *ApJ*, 641, 1060
- Margutti R. et al., 2014, *ApJ*, 780, 21
- Margutti R. et al., 2017, *ApJ*, 835, 140
- Masci F. J. et al., 2019, *PASP*, 131, 018003

- Matheson T., Filippenko A. V., Chornock R., Leonard D. C., Li W., 2000, *AJ*, 119, 2303
- Mauerhan J. C., Filippenko A. V., Zheng W., Brink T. G., Graham M. L., Shivvers I., Clubb K. I., 2018, *MNRAS*, 478, 5050
- Maud J. R. et al., 2011, *ApJ*, 739, L37
- Maud J. R., Smartt S. J., Danziger I. J., 2005, *MNRAS*, 364, L33
- Milislavljevic D. et al., 2015, *ApJ*, 815, 120
- Miller J. S., Stone R. P. S., 1993, *LOTRM*, 66
- Moore A. M., Kasliwal M. M., 2019, *Nature Astron.*, 3, 109
- Morozova V., Piro A. L., Fuller J., Van Dyk S. D., 2020, *ApJ*, 891, L32
- Morozova V., Piro A. L., Renzo M., Ott C. D., Clausen D., Couch S. M., Ellis J., Roberts L. F., 2015, *ApJ*, 814, 63
- Morozova V., Piro A. L., Valenti S., 2018, *ApJ*, 858, 15
- Nakar E., Sari R., 2010, *ApJ*, 725, 904
- Nasa High Energy Astrophysics Science Archive Research Center (Heasarc), 2014, HEASoft: Unified Release of FTOOLS and XANADU. preprint (ascl:1408.004)
- O'Connor E., Ott C. D., 2011, *ApJ*, 730, 70
- Oke J. B. et al., 1995, *PASP*, 107, 375
- Pastorello A. et al., 2007, *Nature*, 447, 829
- Pastorello A. et al., 2008, *MNRAS*, 389, 113
- Pastorello A. et al., 2009, *MNRAS*, 394, 2266
- Piastic A. S., Steele I. A., Bates S. D., Mottram C. J., Smith R. J., Barnsley R. M., Bolton B., 2014, in Ramsay S. K., McLean I. S., Takami H., eds, SPIE Conf. Ser. Vol. 9147, Ground-based and Airborne Instrumentation for Astronomy V. SPIE, Bellingham, p. 91478H
- Poznanski D., Prochaska J. X., Bloom J. S., 2012, *MNRAS*, 426, 1465
- Pumo M. L., Zampieri L., Spiro S., Pastorello A., Benetti S., Cappellaro E., Manicò G., Turatto M., 2017, *MNRAS*, 464, 3013
- Quataert E., Shiode J., 2012, *MNRAS*, 423, L92
- Rest A. et al., 2005, *ApJ*, 634, 1103
- Ricker G. R. et al., 2015, *J. Astron. Telesc. Instr. Syst.*, 1, 014003
- Rodrigo C., Solano E., 2020, in Contributions to the XIV.0 Scientific Meeting (virtual) of the Spanish Astronomical Society. p. 182
- Rodrigo C., Solano E., Bayo A., 2012, SVO Filter Profile Service Version 1.0. IVOA Working Draft
- Roming P. W. A. et al., 2005, *Space Sci. Rev.*, 120, 95
- Schlafly E. F., Finkbeiner D. P., 2011, *ApJ*, 737, 103
- Schlegel E. M., 1990, *MNRAS*, 244, 269
- Shappee B. J. et al., 2014, *ApJ*, 788, 48
- Silverman J. M. et al., 2017, *MNRAS*, 467, 369
- Smartt S. J., 2009, *ARA&A*, 47, 63
- Smartt S. J., 2015, *PASA*, 32, e016
- Smartt S. J., Eldridge J. J., Crockett R. M., Maud J. R., 2009, *MNRAS*, 395, 1409
- Smith N., 2014, *ARA&A*, 52, 487
- Smith N., 2017, *Interacting Supernovae: Types IIin and Ibn*. Handbook of Supernovae. Springer International Publishing AG. p. 403
- Smith N., Hinkle K. H., Ryde N., 2009, *AJ*, 137, 3558
- Smith N., Li W., Filippenko A. V., Chornock R., 2011, *MNRAS*, 412, 1522
- Sollerman J. et al., 2020, *A&A*, 643, A79
- Spiro S. et al., 2014, *MNRAS*, 439, 2873
- STScI Development Team, 2013, pynsphot: Synthetic photometry software package. preprint (ascl:1303.023)
- Sukhbold T., Adams S., 2020, *MNRAS*, 492, 2578
- Sukhbold T., Ertl T., Woosley S. E., Brown J. M., Janka H. T., 2016, *ApJ*, 821, 38
- Szalai T. et al., 2019, *ApJ*, 876, 19
- Tartaglia L. et al., 2021, *ApJ*, 907, 52
- Terreran G. et al., 2016, *MNRAS*, 462, 137
- Terreran G. et al., 2021, preprint (arXiv:2105.12296)
- Theureau G., Hanski M. O., Coudreau N., Hallet N., Martin J. M., 2007, *A&A*, 465, 71
- Thomas R. C., Nugent P. E., Meza J. C., 2011, *PASP*, 123, 237
- Tinyanont S. et al., 2016, *ApJ*, 833, 231
- Tinyanont S. et al., 2019a, *ApJ*, 873, 127
- Tinyanont S. et al., 2019b, *ApJ*, 887, 75
- Tonry J. L. et al., 2018, *PASP*, 130, 064505
- Utrobin V. P., Chugai N. N., 2008, *A&A*, 491, 507
- Valenti S. et al., 2014, *MNRAS*, 438, L101
- Valenti S. et al., 2016, *MNRAS*, 459, 3939
- Valley P. J., Kochanek C. S., Stanek K. Z., Fausnaugh M., Shappee B. J., 2021, *MNRAS*, 500, 5639
- van den Bergh S., Li W., Filippenko A. V., 2005, *PASP*, 117, 773
- Van Dyk S. D. et al., 2014, *AJ*, 147, 37
- Van Dyk S. D. et al., 2019, *ApJ*, 875, 136
- van Dyk S. D., Sramek R. A., Weiler K. W., Panagia N., 1993, *ApJ*, 409, 162
- Virtanen P. et al., 2020, *Nature Meth.*, 17, 261
- Walmswell J. J., Eldridge J. J., 2012, *MNRAS*, 419, 2054
- Woods D. F. et al., 2021, *PASP*, 133, 014503
- Wu S., Fuller J., 2021, *ApJ*, 906, 3
- Yaron O. et al., 2017, *Nature Phys.*, 13, 510
- Zapartas E. et al., 2019, *A&A*, 631, A5
- Zapartas E., de Mink S. E., Justham S., Smith N., Renzo M., de Koter A., 2021, *A&A*, 645, A6
- Zhang J., Gal-Yam A., Wang L., Wang X., Xing L., Yang Y., Schulze S., 2020, *Trans. Name Ser. AstroNote*, 80, 1

## APPENDIX A: DETAILED DATA ANALYSIS FIGURES

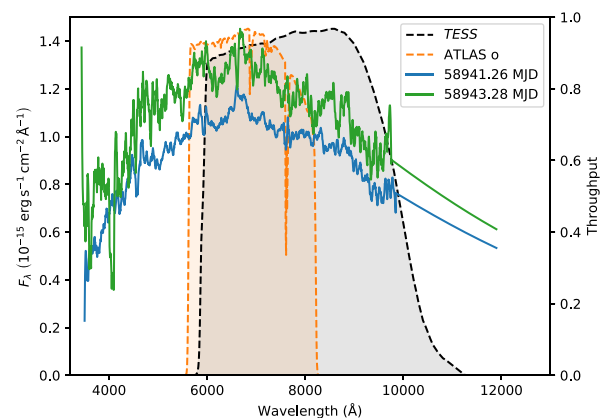


**Figure A1.** Flux calibrated FLOYDS spectra used to calculate the *TESS* synthetic photometry. We extend the spectra to 1200 Å by appending the best fitting blackbody models, to fully cover the *TESS* bandpass. The *TESS* and *ATLAS o*-band passes that are available from SVO are overlaid.

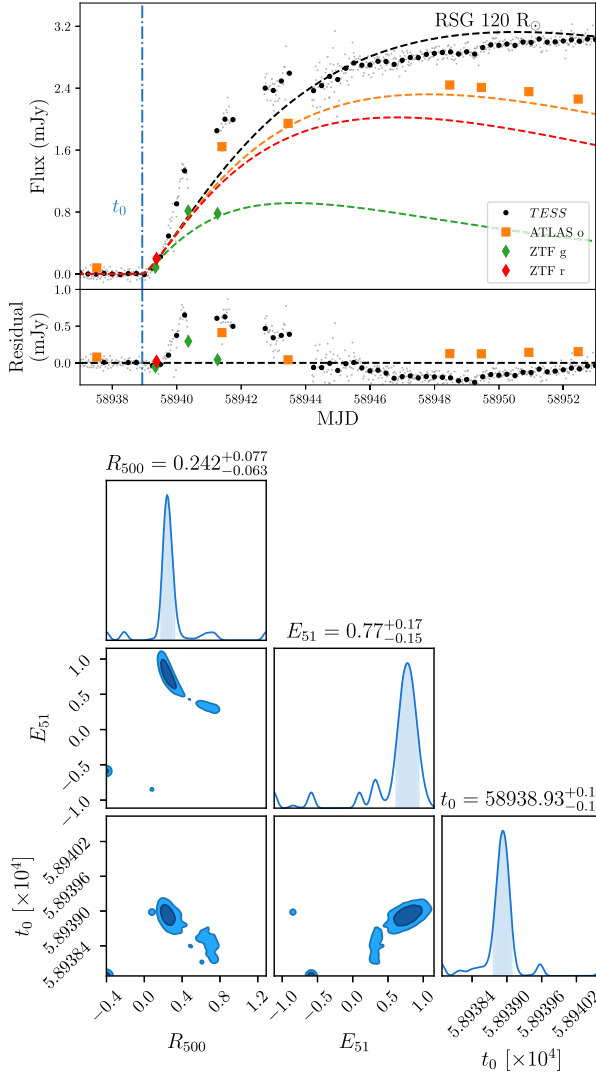


**Figure A2.** Nakar & Sari (2010) analytical RSG model with a progenitor mass of  $15 M_{\odot}$  fit to early photometry. Upper: Early TESS, ATLAS, and ZTF light curves with corresponding light curves derived from the best-fitting parameters. Lower: Parameter distributions from the simultaneous emcee fit to all early photometry, made with `chainconsumer` (Hinton 2016). Although the parameters are well constrained the enhanced brightness at early times due to CSM interaction produces unrealistic physical parameters, therefore, we only use the explosion time,  $t_0$ , from this fit.

<sup>1</sup>Department of Astronomy and Astrophysics, University of California, Santa Cruz, CA 95064, USA

<sup>2</sup>Department of Physics and Astronomy, The Johns Hopkins University, Baltimore, MD 21218, USA

<sup>3</sup>Department of Physics, The Pennsylvania State University, University Park, PA 16802, USA

<sup>4</sup>Center for Interdisciplinary Exploration and Research in Astrophysics (CIERA) and Department of Physics and Astronomy, Northwestern University, Evanston, IL 60208, USA

<sup>5</sup>Department of Physics and Astronomy, Northwestern University, 2145 Sheridan Road, Evanston, IL 60208, USA

<sup>6</sup>School of Physics, Trinity College Dublin, The University of Dublin, Dublin 2, Ireland

<sup>7</sup>Department of Astronomy, University of Illinois at Urbana-Champaign, 1002 W. Green Str, IL 61801, USA

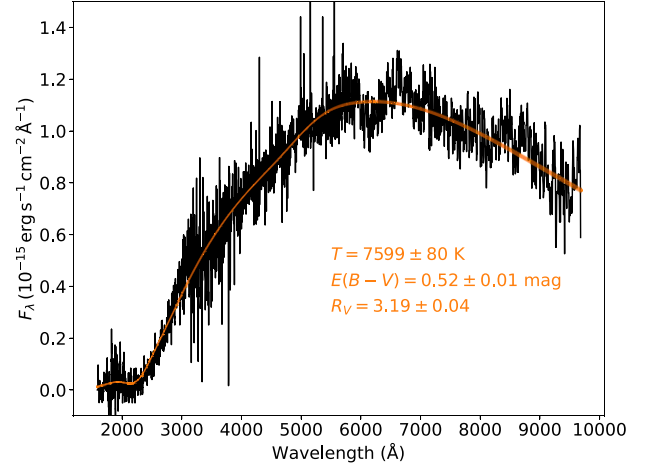


**Figure A3.** HST and ground-based spectroscopy from 4 d post-explosion, where the SN emission is assumed to be well described by a blackbody. We fit this spectrum with a blackbody model to constrain the dust extinction parameters. The resulting best-fitting values are  $E(B - V) = 0.52 \pm 0.01$  mag and  $R_V = 3.19 \pm 0.04$ .

<sup>8</sup>Center for Astrophysical Surveys, National Center for Supercomputing Applications, Urbana, IL, 61801, USA

<sup>9</sup>Department of Physics & Astronomy, Washington State University, Pullman, WA 99164, USA

<sup>10</sup>Space Telescope Science Institute, 3700 San Martin Drive, Baltimore, MD 21218, USA

<sup>11</sup>The Observatories of the Carnegie Institution for Science, 813 Santa Barbara Str, Pasadena, CA 91101, USA

<sup>12</sup>Institute for Astronomy, University of Hawaii, 2680 Woodlawn Drive, Honolulu, HI 96822, USA

<sup>13</sup>Division of Physics, Mathematics and Astronomy, California Institute of Technology, Pasadena, CA 91125, USA

<sup>14</sup>Arkansas Tech University, Russellville, AR 72801, USA

<sup>15</sup>Department of Physics and Astronomy, Rutgers the State University of New Jersey, 136 Frelinghuysen Road, Piscataway, NJ 08854, USA

<sup>16</sup>Instituto de Astrofísica de Canarias, C/Vía Láctea, s/n, E-38205 San Cristóbal de La Laguna, Tenerife, Spain

<sup>17</sup>Universidad de La Laguna, Dpto. Astrofísica, E-38206 San Cristóbal de La Laguna, Tenerife, Spain

<sup>18</sup>Geneva Observatory, University of Geneva, Chemin Pegasi 51, CH-1290 Versoix, Switzerland

<sup>19</sup>Research School of Astronomy and Astrophysics, Australian National University, Canberra, ACT 2611, Australia

<sup>20</sup>Department of Physics and Astronomy, University of Southampton, Highfield, Southampton SO17 1BJ, UK

<sup>21</sup>Department of Astronomy, University of California, Berkeley, CA 94720-3411, USA

<sup>22</sup>Thacher Observatory, Thacher School, 5025 Thacher Rd. Ojai, CA 93023 USA

This paper has been typeset from a  $\text{\TeX}/\text{\LaTeX}$  file prepared by the author.